



ANTICIPATED SKA1 SCIENCE PERFORMANCE

Document Number..... SKA-TEL-SKO-0000818
 Document Type REP
 Revision 01
 Author R. Braun et al.
 Date2017-10-17
 Document Classification..... UNRESTRICTED
 Status.....Released

Name	Designation	Affiliation	Signature	
Authored by:				
SKAO Science Team p.p. Robert Braun	Science Director	SKAO		
			Date:	2017-10-19
Owned by:				
Robert Braun	Science Director	SKAO		
			Date:	2017-10-19
Approved by:				
Robert Braun	Science Director	SKAO		
			Date:	2017-10-19
Released by:				
Alistair McPherson	Head of Project	SKAO		
			Date:	2017-10-19

DOCUMENT HISTORY

Revision	Date Of Issue	Engineering Change Number	Comments
A	2013-08-16	-	First draft release for internal review
01	2017-10-17	-	First Revision Released

DOCUMENT SOFTWARE

	Package	Version	Filename
Word processor	MS Word	Word 2007	SKA-TEL-SKO-0000818-01_SKA1_Science_Perform
Block diagrams			
Other			

ORGANISATION DETAILS

Name	SKA Organisation
Registered Address	Jodrell Bank Observatory Lower Withington Macclesfield Cheshire SK11 9DL United Kingdom Registered in England & Wales Company Number: 07881918
Fax.	+44 (0)161 306 9600
Website	www.skatelescope.org

TABLE OF CONTENTS

1	INTRODUCTION.....	8
1.1	Purpose of the document	8
1.2	Scope of the document.....	8
2	REFERENCES	9
2.1	Applicable documents.....	9
2.2	Reference documents.....	9
3	SKA PERFORMANCE CALCULATIONS	10
3.1	Sensitivity of an SKA1 dish	10
3.2	Sensitivity of a MeerKAT dish	14
3.3	Combined SKA1-Mid Sensitivity.....	14
3.4	SKA1-Low Sensitivity	14
3.5	SKA2 Sensitivity.....	14
4	COMPARISON WITH OTHER TELESCOPES	15
4.1	VLA Sensitivity	15
4.2	ALMA Sensitivity	15
4.3	uGMRT Sensitivity.....	15
4.4	LOFAR Sensitivity	15
5	SENSITIVITY COMPARISON.....	17
6	SURVEY SPEED COMPARISON	17
7	SENSITIVITY AND PSF AS FUNCTION OF ANGULAR SCALE	18
7.1	Sensitivity and PSF Comparison for SKA1-Mid.....	20
7.2	Sensitivity and PSF Comparison for SKA1-Low	22
8	SIMULATED TEST IMAGE COMPARISONS	24
9	WIDE-BAND “CONTINUUM” OBSERVING.....	32
10	IMAGING SENSITIVITY.....	33
11	NON-IMAGING SENSITIVITY	35
11.1	Non-Imaging Sensitivity for SKA1-Low.....	35
11.2	Non-Imaging Sensitivity for SKA1-Mid.....	36
12	ADDITIONAL SKA1-MID FEED SYSTEMS	36
13	APPENDIX A	37
14	APPENDIX B	41

LIST OF FIGURES

Figure 1. Zenith T_{sky} at the SKA1-Mid site for PWV = 5, 10 and 20mm contributions to the atmospheric emission and the 10th, 50th and 90th percentiles of the Galactic foreground brightness. Atmospheric emission is based on the ATM code (RD5) as embedded in CASA..... 11

Figure 2. Zenith opacity at the SKA1-Mid site for PWV = 5, 10 and 20mm contributions to the atmospheric emission. Atmospheric absorption is based on the ATM code (RD5) as embedded in CASA..... 11

Figure 3. Average PWV over the period 2010 – 2015, as derived by Forkman and Conway after RD6, for the SKA1-Mid and VLA sites. The 10th, 50th and 90th percentiles of the PWV distribution are plotted against month of the year. The yearly average values of P10, P50 and P90 for the SKA1-Mid site are 5.8, 10.7 and 19.2 mm. For the VLA site these are 5.7, 9.6 and 14.5 mm.... 12

Figure 4. Current sensitivity model of a single SKA1 dish at elevations near zenith in a direction well away from the Galactic plane (the 10th percentile) and under dry conditions (PWV = 5mm). Solid lines are used to indicate the bands that are part of the currently planned deployment. 12

Figure 5. Zenith T_{sky} at the ALMA site for PWV = 0.5, 2 and 5mm contributions to the atmospheric emission and the 10th, 50th and 90th percentiles of the Galactic foreground brightness. Atmospheric emission is based on the ATM code (RD5) as embedded in CASA..... 16

Figure 6. Zenith opacity at the ALMA site for PWV = 0.5, 2 and 5mm contributions to the atmospheric emission. Atmospheric absorption is based on the ATM code (RD5) as embedded in CASA..... 16

Figure 7. Sensitivity comparison of some existing and planned facilities. For SKA, the feed systems that are not yet planned for deployment are indicated by the dot-dashed line. Dry conditions (PWV \approx 5mm) are assumed for the SKA and VLA sites while the same PWV = 5mm corresponds to poor conditions for the ALMA site. 17

Figure 8. Survey speed comparison of some existing and planned facilities. For SKA, the feed systems that are not yet planned for deployment are indicated by the dot-dashed line. Dry conditions (PWV \approx 5mm) are assumed for the SKA and VLA sites while the same PWV = 5mm corresponds to poor conditions for the ALMA site. 18

Figure 9. The configuration of SKA1-Low on remote scales. Each white symbol depicts a clump of six stations. The bar shows a scale of 30km. The red symbols are used to depict the ASKAP array. 19

Figure 10. The configuration of SKA1-Mid on remote scales. The bar shows a scale of 35km. The white symbols are used to depict the MeerKAT dishes. 20

Figure 11. Monochromatic image performance as function of angular scale for a nominal frequency of 1.4 GHz. The lower panel provides the image sensitivity relative to the natural array sensitivity for images with the most Gaussian possible dirty beam of the indicated FWHM for an 8h tracking observation. The central panel gives the dirty PSF RMS within the central 10x10 FWHM excluding the central positive lobe for an 8h track. The upper panel gives the dirty PSF RMS for a transit snap-shot. The solid blue curves include both the SKA and MeerKAT dishes, while the dashed curves include only the SKA dishes. 21

Figure 12. Broad-band image performance as function of angular scale for a nominal frequency of 1.4 GHz. The lower panel provides the image sensitivity relative to the natural array sensitivity for images with the most Gaussian possible dirty beam of the indicated FWHM for an 8h tracking observation. The central panel gives the dirty PSF RMS within the central 10x10 FWHM excluding the central positive lobe for an 8h track. The upper panel gives the dirty PSF RMS for a transit snap-shot. The solid blue curves include both the SKA and MeerKAT dishes, while the dashed curves include only the SKA dishes. 22

Figure 13. Monochromatic image performance as function of angular scale for a nominal frequency of 140 MHz. The lower panel provides the image sensitivity relative to the natural array

sensitivity for images with the most Gaussian possible dirty beam of the indicated FWHM for an 4h tracking observation. The central panel gives the dirty PSF RMS within the central 10x10 FWHM excluding the central positive lobe for an 8h track. The upper panel gives the dirty PSF RMS for a transit snap-shot. 23

Figure 14. Broad-band image performance as function of angular scale for a nominal frequency of 140 MHz. The lower panel provides the image sensitivity relative to the natural array sensitivity for images with the most Gaussian possible dirty beam of the indicated FWHM for an 4h tracking observation. The central panel gives the dirty PSF RMS within the central 10x10 FWHM excluding the central positive lobe for an 8h track. The upper panel gives the dirty PSF RMS for a transit snap-shot. 24

Figure 15. Test image, derived from the HST Crab Nebula image, for use with low frequency aperture array imaging simulations at 140 MHz. 26

Figure 16. Test image, derived from the HST M83 image, for use with mid frequency dish array imaging simulations at 1.4 GHz. 26

Figure 17. Test image, derived from the HST Ultra-Deep Field image, for use with mid frequency dish array imaging simulations at 14 GHz. 27

Figure 18. Simulated SKA1-Low continuum transit snap-shot dirty image at 140 MHz. 28

Figure 19. Simulated LOFAR continuum transit snap-shot dirty image at 140 MHz. 28

Figure 20. Simulated SKA1-Mid continuum transit snap-shot dirty image at 1.4 GHz. 29

Figure 21. Simulated VLA continuum transit snap-shot A+B+C+D configuration dirty image at 1.4 GHz. 29

Figure 22. Simulated SKA1-Mid continuum transit snap-shot dirty image at 14 GHz. 30

Figure 23. Simulated VLA continuum transit snap-shot A+B+C+D configuration dirty image at 14 GHz. 30

Figure 24. Simulated SKA1-Mid continuum eight-hour track dirty image at 14 GHz. 31

Figure 25. The relative signal-to-noise ratio as function of fractional bandwidth for varying spectral index of the source population. For negative spectral indices (left) the minimum observing frequency is kept fixed, while for positive spectral indices (right) the maximum observing frequency is kept fixed. 32

Figure 26. The tied array sensitivity of SKA1-Low as function of the maximum radius of included stations (left) as well as the sensitivity as function of frequency for two reference radii (right). The model is appropriate for an average elevation within 45 degrees of zenith in a direction well away from the Galactic plane. 35

Figure 27. The tied array sensitivity of SKA1-Mid as function of the maximum radius of included dishes (left) as well as the sensitivity as function of frequency for two reference radii (right). The model is appropriate for elevations near zenith in a direction well away from the Galactic plane (the 10th percentile) and under dry conditions (PWV = 5mm). Solid lines (right) are used to indicate the bands that are part of the currently planned deployment. 36

Figure 28. Sensitivity of an SKA1 dish equipped with SPF Band 1, reproduced from Figure 8 of RD1. 41

Figure 29. Sensitivity of an SKA1 dish equipped with SPF Band 2, reproduced from Figure 21 of RD16. 42

Figure 30. Sensitivity of an SKA1 dish equipped with SPF Band 5a (left) and 5b (right), reproduced from Figures 78 and 79 of RD3 and in the case of the Band 5a feed has been updated by the authors. 42

Figure 31. Overlay of the SKA1 dish (in blue) and MeerKAT dish (in red) sensitivity models with the referenced data. 42

LIST OF TABLES

Table 1. Image sensitivity of SKA1-Low within the indicated frequency bands for spectral line observations (σ_l for $\Delta\nu/\nu_c = 10^{-4}$) and continuum observations (σ_c for $\Delta\nu/\nu_c \approx 0.3$) for an observation of $\Delta\tau = 1$ hour. The range of Gaussian FWHM beam sizes for which the approximate sensitivity value applies is given by θ_{\min} to θ_{\max} . The Gaussian FWHM beam sizes at which a doubling of the image noise from this base level is realised are given by θ'_{\min} and θ'_{\max} . The anticipated confusion noise at a resolution θ_{\min} and ν_c is also listed (following RD17). 34

Table 2. Image sensitivity of SKA1-Mid within the indicated frequency bands for spectral line observations (σ_l for $\Delta\nu/\nu_c = 10^{-4}$) and continuum observations (σ_c for $\Delta\nu/\nu_c \approx 0.3$) for an observation of $\Delta\tau = 1$ hour. The range of Gaussian FWHM beam sizes for which the sensitivity values applies is given by θ_{\min} to θ_{\max} . The Gaussian FWHM beam sizes at which a doubling of the image noise from this base level is realised are given by θ'_{\min} and θ'_{\max} . The grey shading is used to approximately indicate those frequencies that are not yet part of the current deployment plan (ie. between 1.76 and 4.6 GHz as well as above 15.3 GHz). 34

Table 3. The individual SKA1-Low station and the combined SKA1-Low array natural sensitivities from Figure 7 are listed here as function of frequency. The sensitivity is averaged over solid angles within 45 degrees of zenith. 37

Table 4. The individual SKA1-Mid dish and the combined SKA1-Mid array natural sensitivities from Figures 4 and 7 are listed here as function of frequency. The grey shading is used to indicate frequencies that are not yet part of the current deployment plan. Note that the MeerKAT dishes are only assumed to contribute to the array sensitivity within the UHF, L and S Bands as described in Section 3. 38

Table 5. The imaging sensitivity degradation relative to the natural array sensitivity provided by the SKA1-Low and SKA1-Mid array configurations as plotted in Figures 11, 12, 13 and 14 is listed as a function of the FWHM of the most Gaussian possible dirty beam provided by a (4h for Low and 8h for Mid) tracking observation at a reference frequency (140 MHz for Low and 1.4 GHz for Mid). Image attributes at any other frequency can be inferred by a linear scaling to higher or lower angular scales for higher or lower frequencies. The Sens*/Nat columns for SKA1-Mid are relevant for frequencies at which the MeerKAT dishes do not contribute to the array. 40

LIST OF ABBREVIATIONS

AIP.....	Advanced Instrumentation Programme
ALMA.....	Atacama Large Millimetre Array
ATM.....	Atmospheric Transmission of Microwaves
BD	SKA1 Baseline Design
CASA.....	Common Astronomy Software Applications
DM.....	Dispersion Measure
ECMWF.....	European Centre for Medium-range Weather Forecasts
EMI	Electromagnetic Interference
EoR	Epoch of Reionisation
FRB	Fast Radio Burst
FWHM	Full Width Half Maximum
GMRT	Giant Metre-wave Radio Telescope
HPSO	High Priority Science Objective
ISW.....	Integrated Sachs Wolfe effect
JVLA.....	Jansky Very Large Array (or simply VLA)
LOFAR	LOW Frequency ARray
NIP	Non-Image Processing
PDR.....	Preliminary Design Review
PSF	Point Spread Function
PWV	Precipitable Water Vapour
RFI.....	Radio Frequency Interference
RM.....	Rotation Measure
RMS	Root Mean Square
SED	Spectral Energy Distribution
SEFD.....	System Equivalent Flux Density
SKA	Square Kilometre Array
SKAO	SKA Organisation
VLA.....	Very Large Array
VLBI.....	Very Long Baseline Interferometry

1 Introduction

1.1 Purpose of the document

The purpose of this document is to provide current estimates of the scientific performance anticipated for the SKA1 Design Baseline and to put these in the context of other current facilities. It should be noted that the SKA1 Deployment Baseline may deviate in some respects from the Design Baseline as outlined at the link below.

[24th SKA Board Meeting – July 2017](#)

However, it should also be noted, as clearly stated at the same link, that: “Re-instatement of the omitted capabilities, up to the full restoration of the Design Baseline, is planned, either during or after the construction phase, should additional funding become available.” For this reason, any deviations from the Design Baseline are anticipated to be temporary in nature.

1.2 Scope of the document

In this document the basic sensitivity of the SKA1 dishes and stations is quantified based on the most recent design documentation. Additional attributes, such as the site qualities, the survey speed, the sensitivity as a function of angular scale and the imaging quality more generally are also provided. All of these capabilities are placed in the context of other existing and planned facilities based on the best current documentation. Regular updates of this document are planned to track any developments. If readers have suggestions for clarifications or additional content, then they are invited to contact the authors.

2 References

2.1 Applicable documents

The following documents are applicable to the extent stated herein. In the event of conflict between the contents of the applicable documents and this document, **the applicable documents** shall take precedence.

- [AD1] Applicable Document 1
- [AD2] Applicable Document 2

2.2 Reference documents

The following documents are referenced in this document. In the event of conflict between the contents of the referenced documents and this document, **this document** shall take precedence.

- [RD1] SKA-TEL-DSH-0000120-B, "SPF Band 1 Feed Package Selection".
- [RD2] SKA-TEL-DSH-0000020-Rev2, "SPF Band 2 Design".
- [RD3] SKA-TEL-DSH-0000118, "SPF345 Preliminary Design Document".
- [RD4] 316-000000-022-RevA, "Dish Structure Detail Design".
- [RD5] Pardo et al. 2001, IEEE TransAntProp 49, 1683, "ATM, An improved model for mm/sub-mm applications"
- [RD6] Alshawaf et al., 2017, Atmos.Meas.Tech.Discuss., doi: 10.5194/amt-2017-69, "Estimating trends in atmospheric water vapor and temperature time series over Germany"
- [RD7] MeerKAT Array Releases and Specifications - 2016-10-10
- [RD8] VLA Observational Status Summary
- [RD9] ALMA Cycle 5 Technical Handbook
- [RD10] SKA1 LOW antenna candidates V5.
- [RD11] Lal, Gupta and Chandra, 7 November 2016, private communication.
- [RD12] Nijboer, Pandey-Pommier and De Bruyn, SKA Memo 113, "LOFAR imaging capabilities and system sensitivity"
- [RD13] SKA-TEL-SKO-0000645, "Survey Performance Calculations"
- [RD14] Mancuso, C., et al., 2017, ApJ 842, 95.
- [RD15] Hayward, R.H., 2012, Synthesis Imaging Workshop, "Antennas & Receivers in Radio Astronomy", 31 May 2012, p.50
- [RD16] SKA-TEL-DSH-0000034_1, "Shaping the SKA MID Optics".
- [RD17] Condon, J.J. et al. 2012, ApJ 758, 23.

3 SKA Performance Calculations

3.1 Sensitivity of an SKA1 dish

The sensitivity of a dish can be expressed as the effective collecting area, A_{eff} , divided by the total system temperature, T_{sys} .

The effective collecting area can be expressed as, $A_{\text{eff}} = A_{\text{phys}} \eta_A$, the product of the physical antenna aperture with an aperture efficiency, η_A . The aperture efficiency can in turn be expressed as the product of several contributing factors, most notably the feed illumination efficiency, η_F , the phase efficiency, η_{ph} , of the reflector surface, and a term to capture the large diffractive losses at the lowest frequencies where the reflectors might only be a small number of wavelengths in diameter, η_D , giving $\eta_A = \eta_F \eta_{\text{ph}} \eta_D$. In general, all of these factors will vary with frequency.

Extensive simulations and a smaller number of prototype measurements are presented in the DSH consortium PDR documentation, (RD1, RD2, RD3). The most relevant performance data from these references are gathered together in Appendix B. A simple empirical model for η_F and η_D that captures the dependencies and provides numerical agreement over the frequency ranges of relevance is $\eta_F = 0.92 - 0.04 | \log_{10}(v_{\text{GHz}}) |$ and $\eta_D = 1 - 20 (\lambda/D)^{3/2}$, in terms of the observing frequency in GHz, v_{GHz} , the wavelength, λ , and the dish diameter, D . The phase efficiency can be expressed as $\eta_{\text{ph}} = \exp(-\Delta_{\text{ph}}^2)$, where $\Delta_{\text{ph}} = 2\pi\delta/\lambda$, and $\delta = 2(A_p \epsilon_p^2 + A_s \epsilon_s^2)^{1/2}$. The anticipated RMS surface errors of the primary and secondary reflector surfaces, $\epsilon_p = 280 \mu\text{m}$ and $\epsilon_s = 154 \mu\text{m}$, as well as the constants appropriate for the design optics, $A_p = 0.89$ and $A_s = 0.98$, are provided in RD4.

The system temperature can be expressed approximately as,

$$T_{\text{sys}} = (T_{\text{rcv}} + T_{\text{spl}} + T_{\text{sky}})_x / \exp[-\tau_0 \sec(z)],$$

in terms of the receiver temperature, T_{rcv} , the spill-over temperature, T_{spl} , the sky temperature, T_{sky} , the atmospheric zenith opacity, τ_0 , and the zenith angle, z . The subscript “x” to the temperature term is used to indicate that a correction of the form $T_x = T \{ (hv/kT) / [\exp(hv/kT) - 1] \}$ is applied. The sky temperature can be expressed as $T_{\text{sky}} = T'_{\text{cmb}} + T'_{\text{gal}} + T_{\text{atm}}$, the sum of CMB, Galactic and atmospheric contributions. T_{cmb} is simply 2.73 K. T_{gal} depends on the pointing direction of the telescope and can be approximated, away from the Galactic plane, where thermal free-free emission is minimal, with $T_{\text{gal}} = T_{408} (0.408/v_{\text{GHz}})^{2.75}$ K. The leading constant has values of $T_{408} = 17.1, 25.2$ and 54.8 K for the 10th, 50th and 90th percentile of the all-sky distribution, when gridded in an equal area projection. The primed quantities, T'_{cmb} and T'_{gal} , are attenuated by the atmospheric absorption, $\exp[-\tau_0 \sec(z)]$. The atmospheric contribution depends on the site and weather attributes, specifically the site elevation, atmospheric pressure and zenith water vapour content, together with the zenith angle of an observation. We use the ATM code of RD5 as implemented within CASA with its default atmospheric profile parameters, together with a representative elevation (near the core of the array) of 1100m, ambient temperature of 290K and atmospheric pressure of 895 mbar to calculate the zenith atmospheric emission and opacity at the SKA1-Mid site at three indicative values of the precipitable water vapour of 5, 10 and 20mm. These are shown in Figures 1 and 2.

Weather statistics from the ECMWF for the SKA1-Mid site over the interval 2010 – 2015 have been used to estimate the PWV as function of month of the year by Peter Forkman and John Conway using the methodology described in RD6 and the 10th, 50th and 90th percentiles of those distributions are plotted in Figure 3 together with the same curves for the VLA site. The yearly average values of P10, P50 and P90 for the SKA1-Mid are 5.8, 10.7 and 19.2 mm. For comparison, we note that for the VLA site these are 5.7, 9.6 and 14.5 mm.

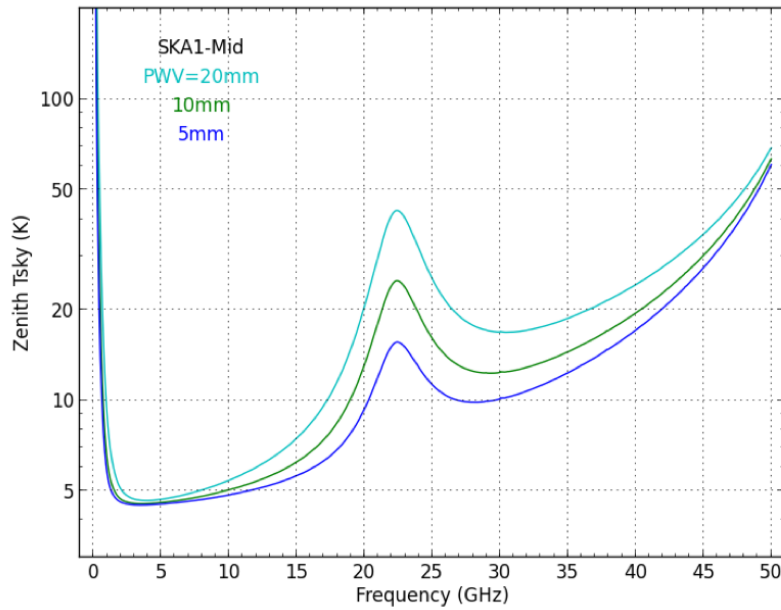


Figure 1. Zenith T_{sky} at the SKA1-Mid site for PWV = 5, 10 and 20mm contributions to the atmospheric emission and the 10th, 50th and 90th percentiles of the Galactic foreground brightness. Atmospheric emission is based on the ATM code (RD5) as embedded in CASA.

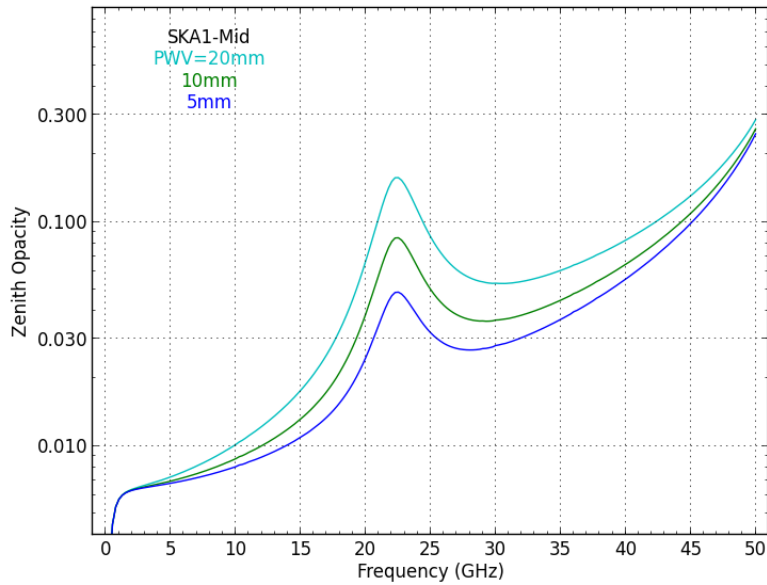


Figure 2. Zenith opacity at the SKA1-Mid site for PWV = 5, 10 and 20mm contributions to the atmospheric emission. Atmospheric absorption is based on the ATM code (RD5) as embedded in CASA.

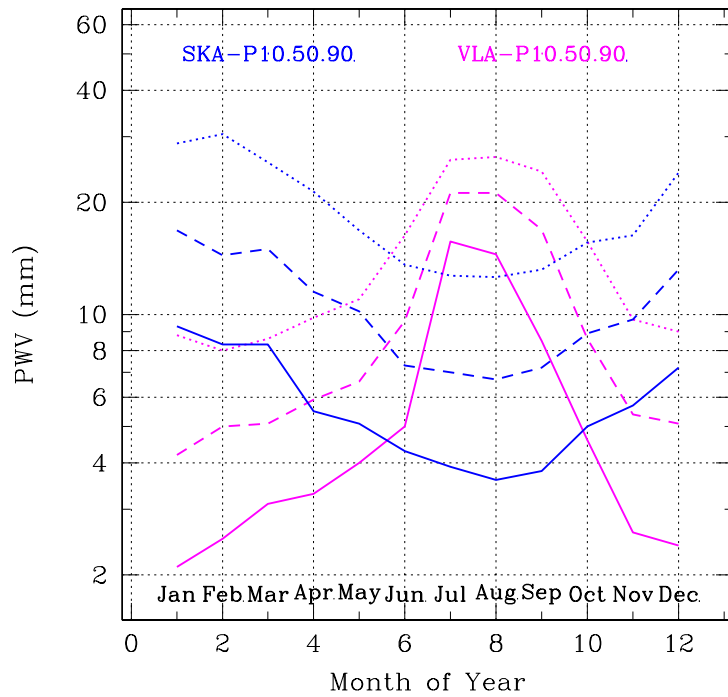


Figure 3. Average PWV over the period 2010 – 2015, as derived by Forkman and Conway after RD6, for the SKA1-Mid and VLA sites. The 10th, 50th and 90th percentiles of the PWV distribution are plotted against month of the year. The yearly average values of P10, P50 and P90 for the SKA1-Mid site are 5.8, 10.7 and 19.2 mm. For the VLA site these are 5.7, 9.6 and 14.5 mm.

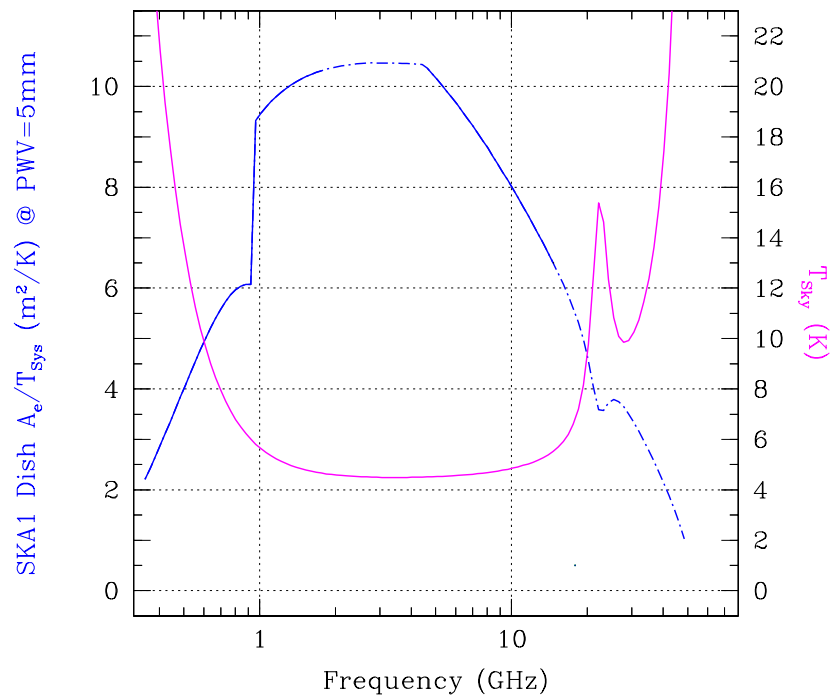


Figure 4. Current sensitivity model of a single SKA1 dish at elevations near zenith in a direction well away from the Galactic plane (the 10th percentile) and under dry conditions (PWV = 5mm). Solid lines are used to indicate the bands that are part of the currently planned deployment.

The SKA offset Gregorian shaped dish design, with its “feed down” geometry and extended secondary reflector provides very low spill-over temperatures for zenith angles within about 45 degrees of zenith. Current indications are that the optimised “octave band” feeds being deployed at 950 MHz and above should provide $T_{\text{spl}} \approx 3$ K. The 3:1 bandwidth Quad-Ridge Feed Horn design being used for Band 1 (350 – 1050 MHz) is likely to have a higher T_{spl} , but for simplicity we will assume a constant value of $T_{\text{spl}} = 3$ K at all frequencies and capture the documented variation of sensitivity performance with frequency within Band 1 in our model of T_{rcv} .

We model T_{rcv} for each of the SKA1-Mid bands guided both by the published T_{rcv} models within the PDR documentation as well as the simulations that yield the final values of $A_{\text{eff}}/T_{\text{sys}}$ as documented in RD1 – RD4. For the various bands, this yields:

Band 1 (0.35 – 1.05 GHz): $T_{\text{rcv}} = 15 + 30 (v_{\text{GHz}} - 0.75)^2$ K

Band 2, 3, 4 (0.95 – 4.6 GHz): $T_{\text{rcv}} = 7.5$ K

Band 5+ (4.6 – 50 GHz): $T_{\text{rcv}} = 4.4 + 0.69 v_{\text{GHz}}$ K

As already noted, the T_{rcv} model, particularly for Band 1, is used to capture several effects in order to reproduce the appropriate $A_{\text{eff}}/T_{\text{sys}}$. The model at higher frequencies (> 16 GHz) is deliberately conservative, as it represents an extrapolation beyond what has received study. For comparison, Bob Hayward of NRAO has shown [RD15] that the model $T_{\text{rcv}} = 2 + 0.5 v_{\text{GHz}}$ K represents a plausible target for $v_{\text{GHz}} = 4 - 50$ GHz.

The combined model for the sensitivity of a single SKA1 dish is illustrated in Figure 4. The sky temperature is based on the 10th percentile of the Galactic foreground brightness distribution and toward the zenith under dry conditions (PWV = 5mm) which should be available about 10% of the time at the SKA1-Mid site. The values in Figure 4 are compared directly with those in the simulations presented in RD1 – RD4 in Appendix B. A table providing the values plotted in Figure 4 is included in Appendix A as Table 4.

3.2 Sensitivity of a MeerKAT dish

A similar model to the one described above for the SKA dishes can be defined for the MeerKAT dishes. The feed and diffraction efficiencies are modelled as, $\eta_F = 0.80 - 0.04 | \log_{10}(v_{\text{GHz}}) |$ and $\eta_D = 1 - 20 (\lambda/D)^{3/2}$. The phase efficiency is calculated as before, but the RMS surface errors of the primary and secondary reflector surfaces are assumed to be, $\epsilon_p = 480 \mu\text{m}$ and $\epsilon_s = 265 \mu\text{m}$, to be consistent with a total surface accuracy of about $600 \mu\text{m}$ RMS (from RD7). We assume $T_{\text{spl}} = 4 \text{ K}$ and model T_{rcv} as:

Band UHF (0.58 – 1.02 GHz): $T_{\text{rcv}} = 11 - 4.5 (v_{\text{GHz}} - 0.58) \text{ K}$

Band L (0.9 – 1.67 GHz): $T_{\text{rcv}} = 7.5 + 6.8 (| v_{\text{GHz}} - 1.65 |)^{3/2} \text{ K}$

Band S (1.65 – 3.05 GHz): $T_{\text{rcv}} = 7.5 \text{ K}$.

This model has been calibrated against the on-sky L-Band measurements reported in RD7 as shown in Appendix B. The UHF and S-Band models should be regarded as preliminary.

3.3 Combined SKA1-Mid Sensitivity

The combined sensitivity of SKA1-Mid, including both the 133 SKA1 15m dishes as well as the 64 MeerKAT 13.5m dishes is given by the sum of $A_{\text{eff}}/T_{\text{sys}}$ over all dishes and is listed in Table 4. As noted above, the MeerKAT dishes are only assumed to contribute in the UHF, L and S bands. This combined sensitivity will be relevant for imaging applications as discussed further in Section 10. Non-imaging applications will generally make use of a sub-set of the total number of dishes as discussed further in Section 11.

3.4 SKA1-Low Sensitivity

The antenna that will be used within the SKA1-Low stations is currently under review. As a placeholder, we will consider the sensitivity parameters provided in RD10 for what is termed the SKALA4_BT16 design as deployed within stations having a 40m diameter and each consisting of 256 randomly distributed antennas. The values that will be plotted are for 512 stations and are averaged over all solid angles within 45deg of zenith and are referenced to an assumed Galactic foreground contribution with, $T_{408} = 20 \text{ K}$. As noted previously, this corresponds to a value between the 10th and 50th percentile of the all-sky distribution and would apply to directions well away from the Galactic plane. The total array sensitivity will be relevant for imaging applications as discussed further in Section 10. Non-imaging applications will generally make use of a sub-set of the total number of stations as discussed further in Section 11.

3.5 SKA2 Sensitivity

While the detailed scope of SKA2 must still be determined, performance projections are currently based on an assumed deployment of 2000 SKA1 15m dishes that are equipped with two Phased Array Feeds to cover 0.35 – 1.67 GHz and octave band feeds between 1.65 and 50 GHz, together with 4880 SKA1 40m diameter low frequency stations that provide performance between 50 and 350 MHz.

4 Comparison with other telescopes

It is interesting to compare the performance of the SKA with that of other telescopes.

4.1 VLA Sensitivity

The System Equivalent Flux Density (SEFD) of the recently upgraded Jansky Very Large Array (JVLA or simply VLA) antennas is provided in the Observational Status Summary as function of frequency in RD8. The SEFD is related to $A_{\text{eff}}/T_{\text{sys}}$ by, $\text{SEFD} = 2 k_B T_{\text{sys}}/A_{\text{eff}}$, for the Boltzmann constant k_B . The high frequency parameters are appropriate for dry conditions and are corrected for atmospheric opacity at the zenith.

4.2 ALMA Sensitivity

The lowest frequency bands of ALMA overlap with the range accessible to the SKA1. The ALMA interferometric array consists of 50 dishes of 12m diameter and 12 dishes of 7m diameter. The sensitivity is calculated following RD9, the ALMA Cycle 5 Technical Handbook, using equations 9.7 and 9.8, together with Table 9.2 from that reference. As previously, we calculate the sky temperature and opacity for the ALMA site, at an assumed elevation of 5100m, ambient temperature of 268 K and atmospheric pressure of 555 mbar. The fiducial water vapour levels for the calculation were taken to be PWV = 0.5, 2 and 5mm, which correspond approximately to the 10th, 50th and 90th percentiles of the PWV distribution at the ALMA site. The atmospheric emission and absorption for the ALMA site are shown in Figures 5 and 6. The ALMA Bands 3 and 1 frequencies are indicated with solid lines in the plots, since Band 3 is already available and Band 1 deployment is anticipated during 2019/2020. The ALMA Band 2 frequency range is indicated with a dot-dash line in the plots, since it has not yet been funded for deployment.

4.3 uGMRT Sensitivity

The anticipated performance of the upgraded GMRT array, consisting of 30 dishes of 45m diameter has been provided by Lal, Gupta and Chandra (RD11). Four feed systems together provide frequency coverage from 120 – 1390 MHz.

4.4 LOFAR Sensitivity

The theoretical LOFAR sensitivity has been calculated following the prescription given by Nijboer, Pandey-Pommier and De Bruyn in RD12.

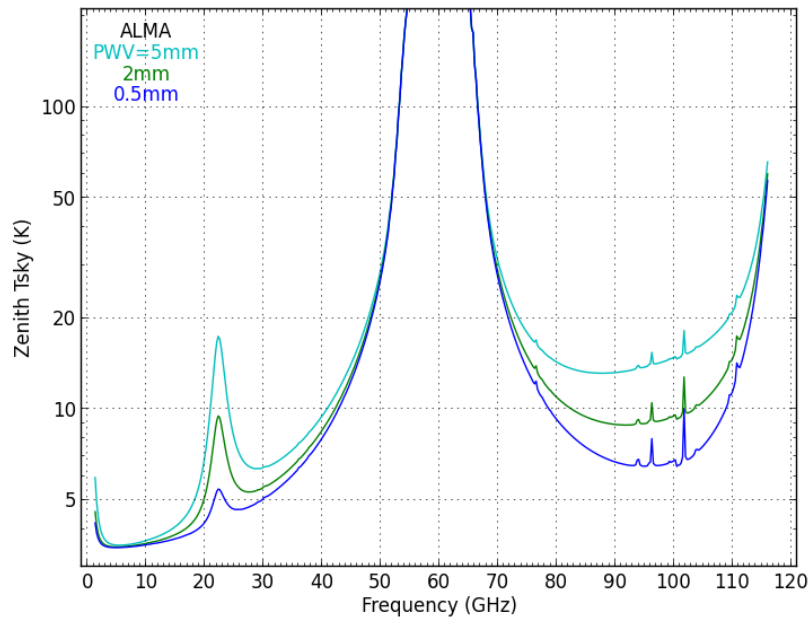


Figure 5. Zenith T_{sky} at the ALMA site for PWV = 0.5, 2 and 5mm contributions to the atmospheric emission and the 10th, 50th and 90th percentiles of the Galactic foreground brightness. Atmospheric emission is based on the ATM code (RD5) as embedded in CASA.

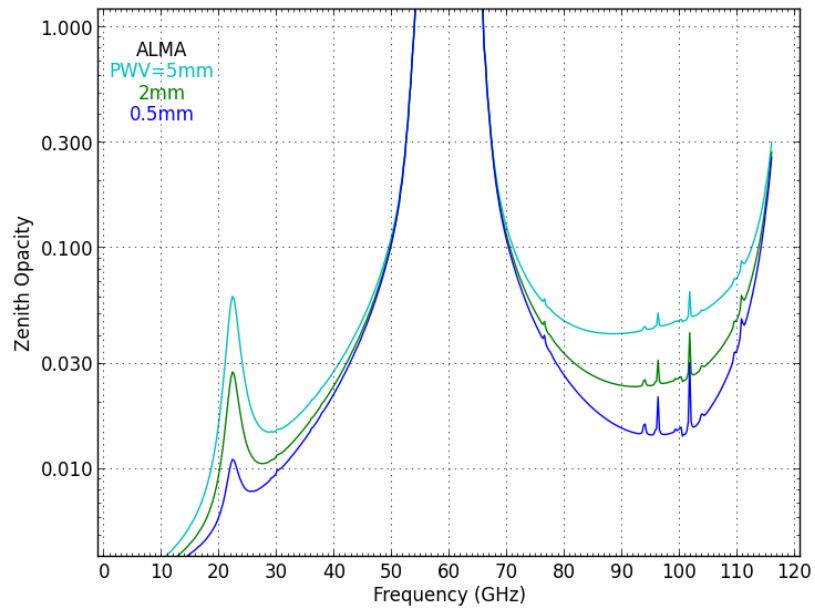


Figure 6. Zenith opacity at the ALMA site for PWV = 0.5, 2 and 5mm contributions to the atmospheric emission. Atmospheric absorption is based on the ATM code (RD5) as embedded in CASA.

5 Sensitivity Comparison

The sensitivity of the SKA is compared to various existing and planned facilities in Figure 7 based on the values documented in Sections 3 and 4 above.

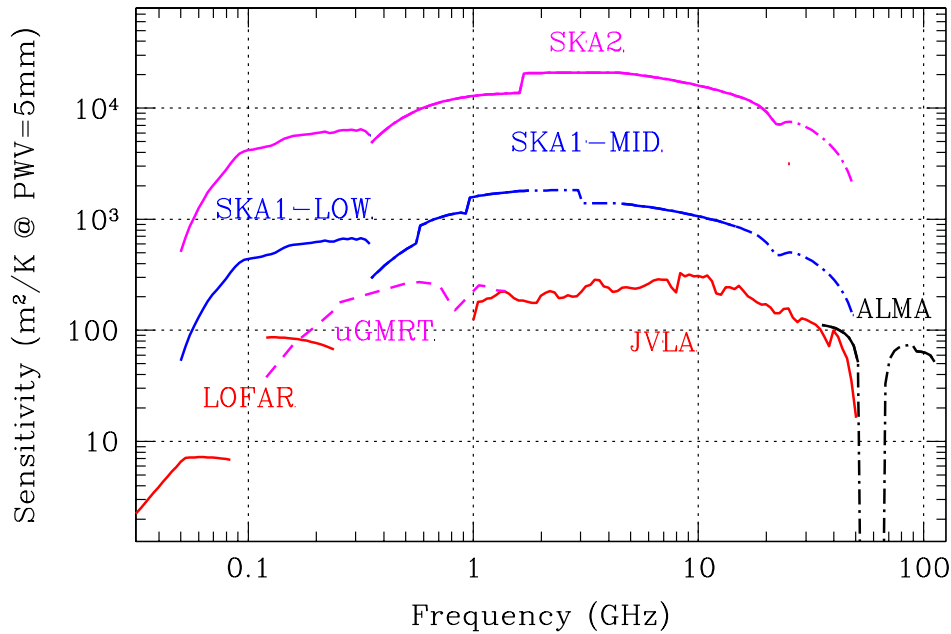


Figure 7. Sensitivity comparison of some existing and planned facilities. For SKA, the feed systems that are not yet planned for deployment are indicated by the dot-dashed line. Dry conditions ($PWV \approx 5\text{mm}$) are assumed for the SKA and VLA sites while the same $PWV = 5\text{mm}$ corresponds to poor conditions for the ALMA site.

6 Survey Speed Comparison

The survey speed, SS , can be expressed as the product of sensitivity squared with the noise effective Field of View, $SS = S^2 \text{FoV}_{\text{eff}}$. The noise effective FoV_{eff} is provided by the integral of the square of the normalised primary beam pattern. For the case of a dish with a 10 dB edge taper to the illumination pattern this is given approximately $\text{FoV}_{\text{eff}} = 2340 (\lambda/D)^2 \text{deg}^2$, in terms of the observing wavelength, λ , and dish diameter, D . For the case of a uniformly illuminated aperture (such as an aperture array that is beam-formed for maximum sensitivity) one has instead, $\text{FoV}_{\text{eff}} = 1920 (\lambda/D)^2 \text{deg}^2$.

The survey speed of the SKA is compared to various existing and planned facilities in Figure 8 based on the sensitivity values documented in Sections 3 and 4 above, together with the dish or station diameters noted there. In those case where multiple dish diameters contribute to the array, only the largest is used in the calculation. The FoV_{eff} for the special case of Phased Array Feeds (assumed in the SKA2 deployment) is described in RD13.

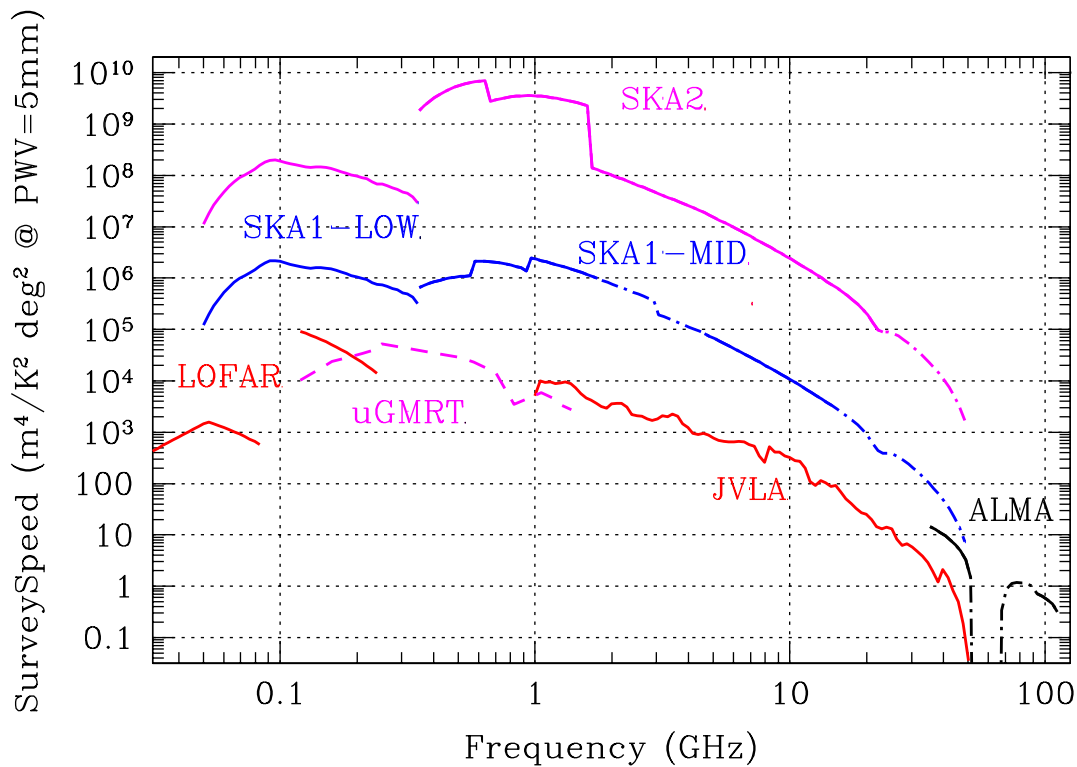


Figure 8. Survey speed comparison of some existing and planned facilities. For SKA, the feed systems that are not yet planned for deployment are indicated by the dot-dashed line. Dry conditions ($PWV \approx 5\text{mm}$) are assumed for the SKA and VLA sites while the same $PWV = 5\text{mm}$ corresponds to poor conditions for the ALMA site.

7 Sensitivity and PSF as function of Angular Scale

The basic observing mode that is employed for an imaging experiment with an array of dishes or aperture array stations varies between one (or more) short snap-shots to a more extensive sky-tracking observation. Since the visibility sampling is improved with long duration tracks, we will consider as one extreme, the longest practical tracks consistent with good performance for the type of receptor being employed, namely 8 hour tracks that extend from -4 h to $+4\text{ h}$ of Hour Angle for the dish arrays and 4 hour tracks, extending from -2 h to $+2\text{ h}$ for the aperture arrays. While the character and quality of the visibility coverage are also influenced to some degree by the Declination of the field being observed, we will concentrate on the middle of the accessible Dec. range near -30° (or $+30^\circ$ for the Northern comparison facilities) as an illustrative example. Generally, the coverage will become even more symmetric and complete for more negative Declinations, while Declinations near 0 are the most limited. At the other extreme from the long tracks, we will consider the case of a single snap-shot observation near transit.

Further, we will consider both “spectral line” and “continuum” observing modes, with “spectral line” providing essentially monochromatic visibilities, and with “continuum” being defined as constituting a 30% fractional bandwidth that is simulated with 30 spectral channels each of 1% width. There are various reasons why mixing larger fractional bandwidths into a single image may not be very meaningful, and we consider this question in more detail in Section 9 below. However, it should of course be noted that under many circumstances it will be possible to acquire more than 30%

fractional bandwidth simultaneously and the larger the instantaneous bandwidth, the greater the scientific utility in general.

The three basic image quality attributes that will be generated are (1) the relative sensitivity, as well as (2) the RMS near-in sidelobe level of the full-track or (3) the snap-shot synthesized beam, all as a function of the angular scale. Near-in sidelobe levels are measured within the central 10x10 FWHM of the synthesized beam, excluding the PSF main lobe down to the first null itself. To probe the response to different angular scales, all of the visibility data are first gridded with a so-called “uniform” weighting that is tied to a support function that spans the smaller of: 512x512 times the target FWHM of a specific imaging simulation, or 4x4 times the primary beam FWHM. Subsequently, the visibilities are tapered with a Gaussian taper that matches the specific target FWHM, prior to forming the dirty image and PSF. In this way, target Gaussian FWHM that logarithmically sample (in multiples of between 1.5 and 2) the entire range of angular scales for which the array configuration has any sensitivity are systematically probed. The target FWHM is in all cases sampled with 4x4 image pixels. The RMS noise level in each dirty image is compared to the RMS noise level of those same visibilities when gridded and imaged with “natural” weighting. Although the imaging simulations are all carried out at a single nominal reference frequency, the image attributes at any other frequency can be inferred by a linear scaling to higher or lower angular scales for higher or lower frequencies. It is only the underlying “natural” sensitivity of the array as function of frequency that need also be known to fully specify the imaging performance and this has already been tabulated in Sections 3 and 4.

The array configurations for SKA1-Low and SKA1-Mid are shown in Figures 9 and 10. Since the MeerKAT dishes are only equipped with feeds for a portion the frequency coverage of SKA1-Mid, the imaging simulations are shown both with, and with-out, inclusion of the 64 MeerKAT dishes.

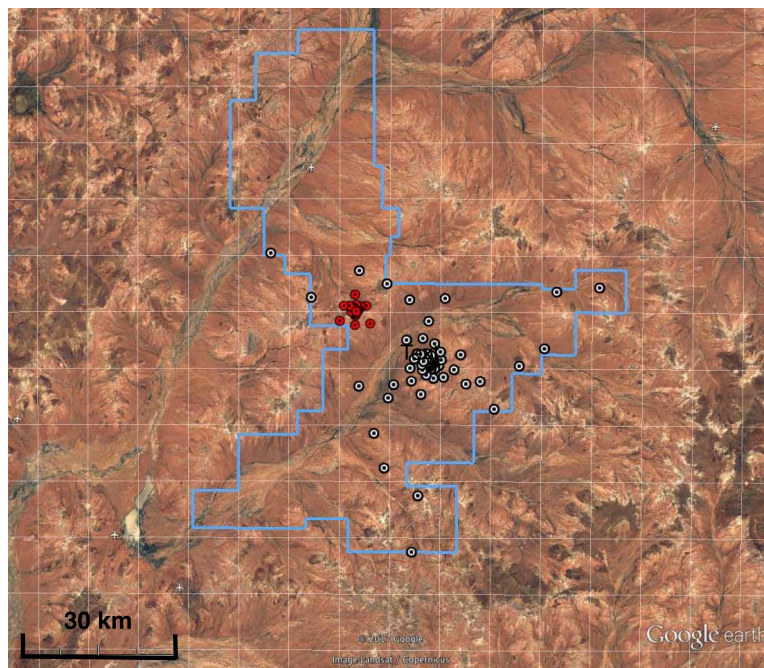


Figure 9. The configuration of SKA1-Low on remote scales. Each white symbol depicts a clump of six stations. The bar shows a scale of 30km. The red symbols are used to depict the ASKAP array.

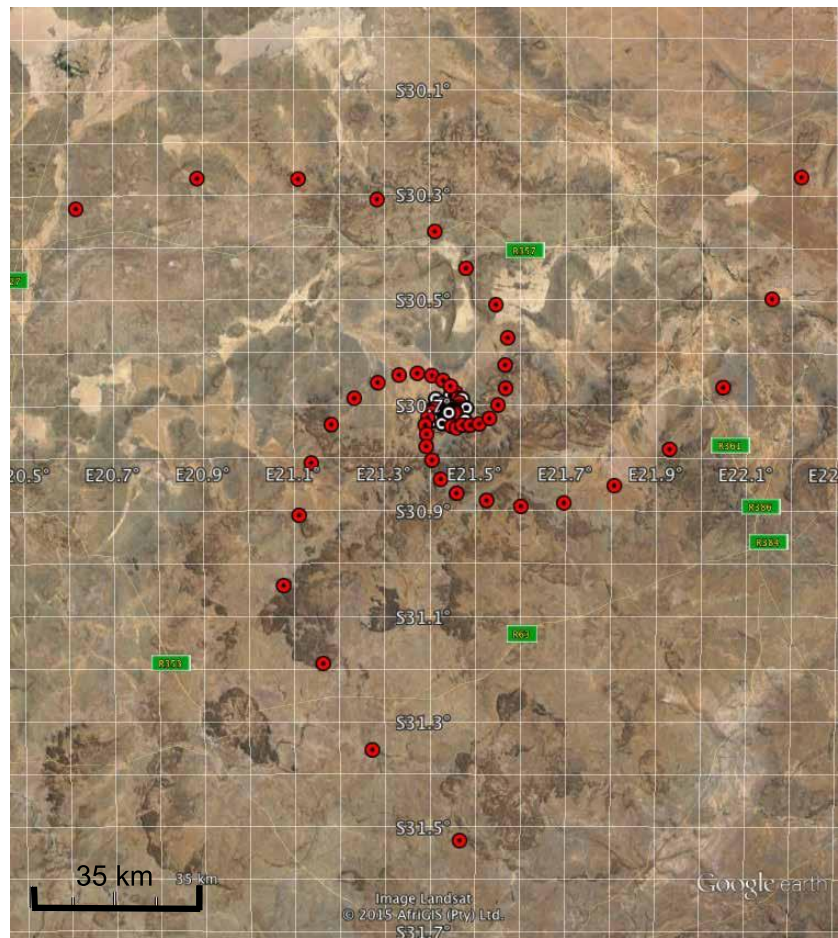


Figure 10. The configuration of SKA1-Mid on remote scales. The bar shows a scale of 35km. The white symbols are used to depict the MeerKAT dishes.

7.1 Sensitivity and PSF Comparison for SKA1-Mid

The image quality attributes of SKA1-Mid are compared to those of the four VLA configurations for spectral line and broad-band continuum observations in Figures 11 and 12.

Monochromatic Imaging Performance

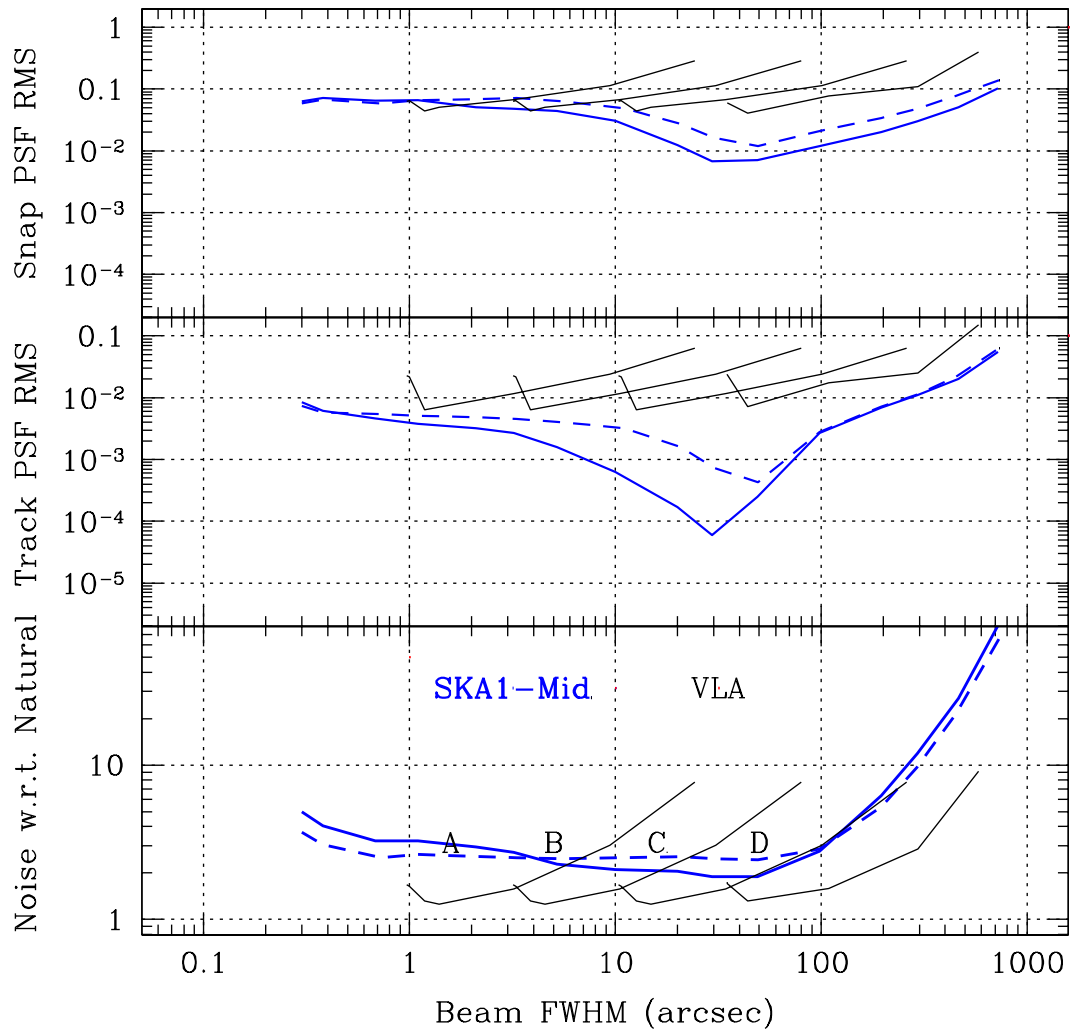


Figure 11. Monochromatic image performance as function of angular scale for a nominal frequency of 1.4 GHz. The lower panel provides the image sensitivity relative to the natural array sensitivity for images with the most Gaussian possible dirty beam of the indicated FWHM for an 8h tracking observation. The central panel gives the dirty PSF RMS within the central 10x10 FWHM excluding the central positive lobe for an 8h track. The upper panel gives the dirty PSF RMS for a transit snap-shot. The solid blue curves include both the SKA and MeerKAT dishes, while the dashed curves include only the SKA dishes.

Continuum ($\Delta\nu/\nu=0.3$) Imaging Performance

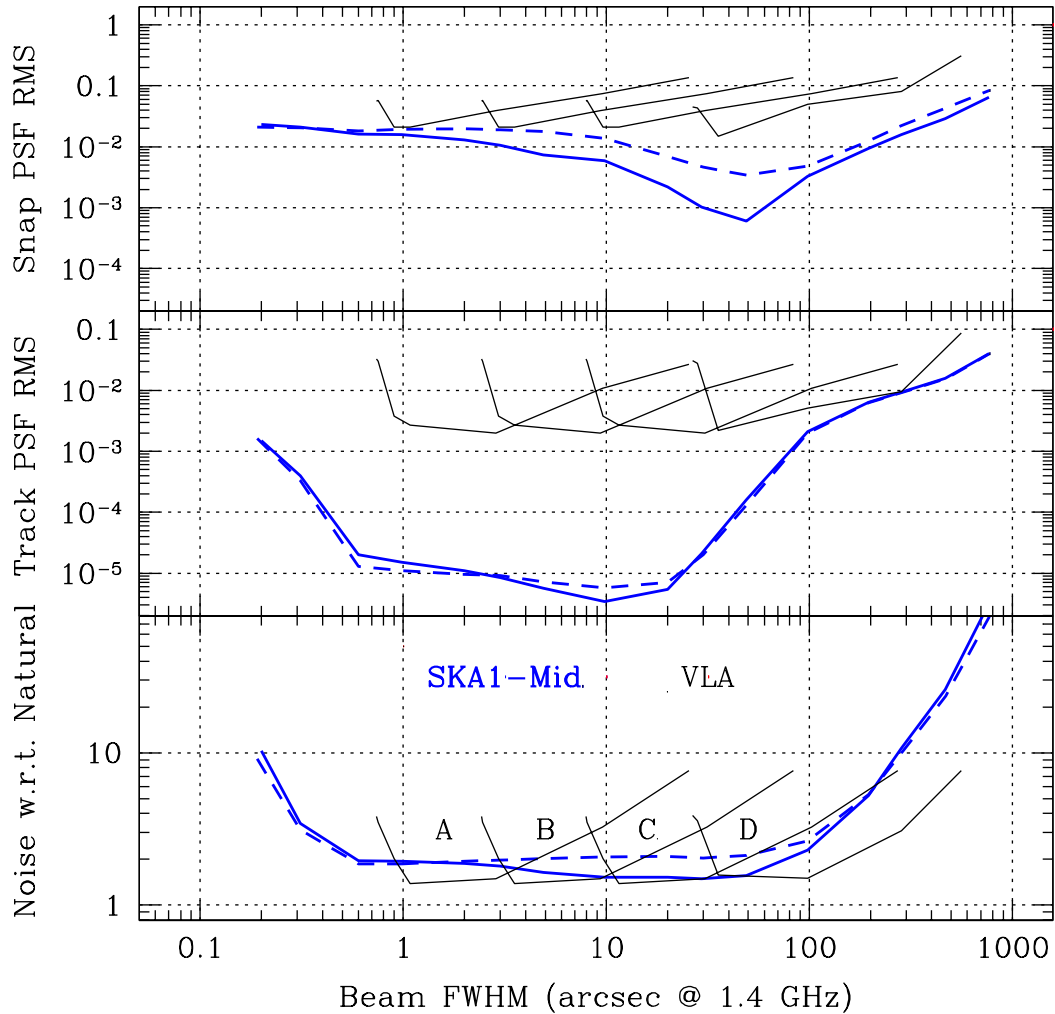


Figure 12. Broad-band image performance as function of angular scale for a nominal frequency of 1.4 GHz. The lower panel provides the image sensitivity relative to the natural array sensitivity for images with the most Gaussian possible dirty beam of the indicated FWHM for an 8h tracking observation. The central panel gives the dirty PSF RMS within the central 10x10 FWHM excluding the central positive lobe for an 8h track. The upper panel gives the dirty PSF RMS for a transit snap-shot. The solid blue curves include both the SKA and MeerKAT dishes, while the dashed curves include only the SKA dishes.

7.2 Sensitivity and PSF Comparison for SKA1-Low

The image quality attributes of SKA1-Low are compared to those of LOFAR for spectral line and broad-band continuum observations in Figures 13 and 14.

Monochromatic Imaging Performance

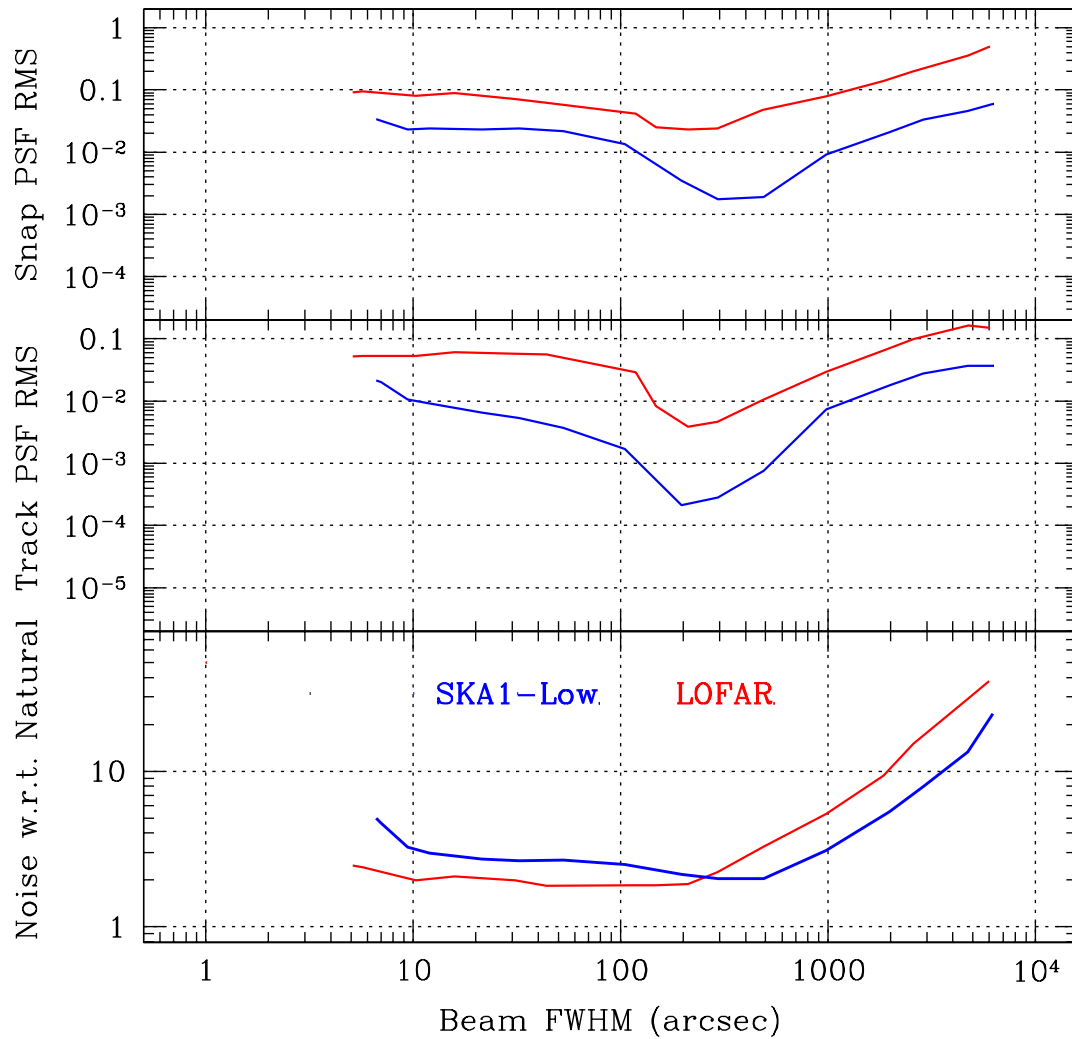


Figure 13. Monochromatic image performance as function of angular scale for a nominal frequency of 140 MHz. The lower panel provides the image sensitivity relative to the natural array sensitivity for images with the most Gaussian possible dirty beam of the indicated FWHM for an 4h tracking observation. The central panel gives the dirty PSF RMS within the central 10x10 FWHM excluding the central positive lobe for an 8h track. The upper panel gives the dirty PSF RMS for a transit snap-shot.

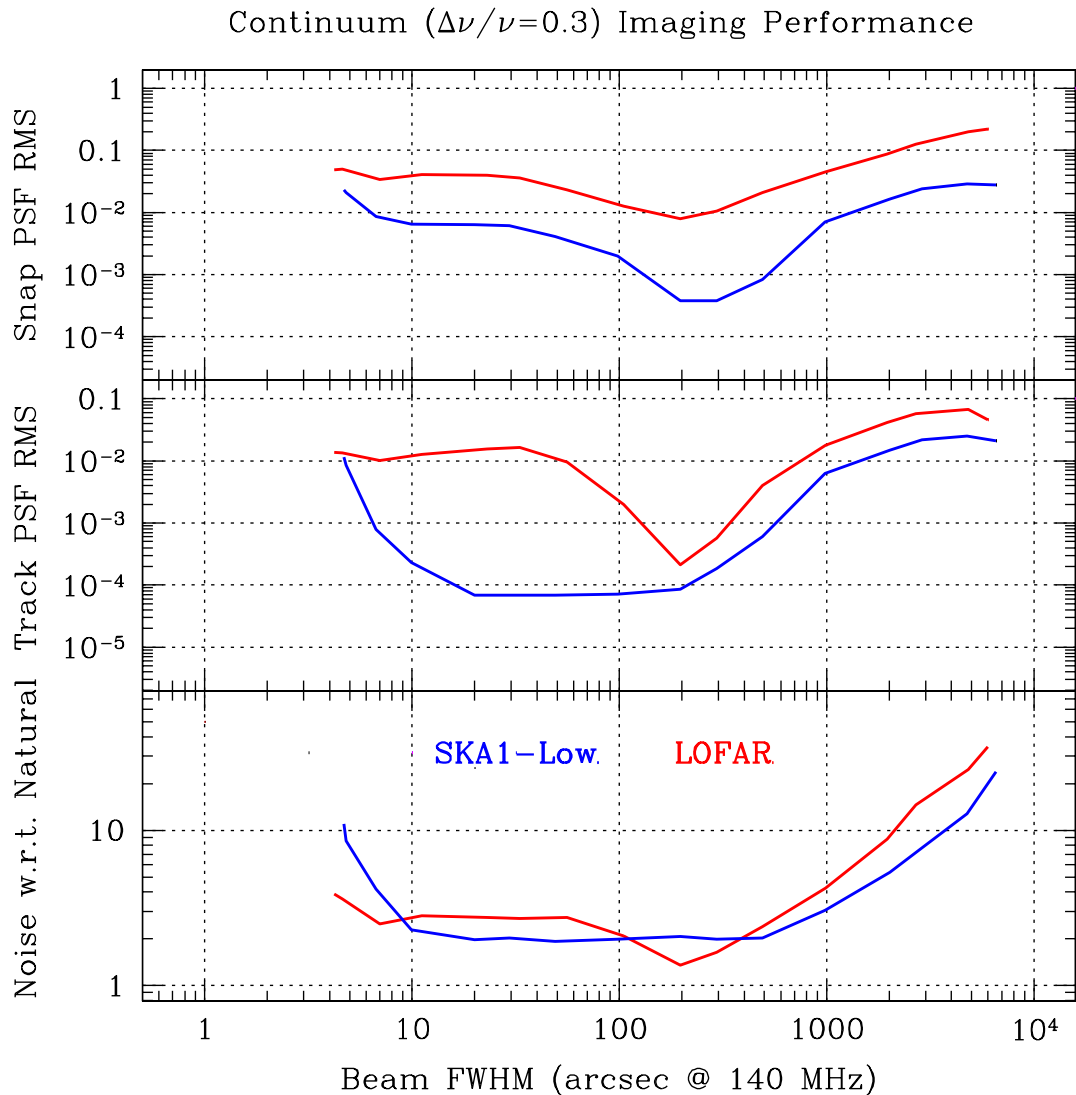


Figure 14. Broad-band image performance as function of angular scale for a nominal frequency of 140 MHz. The lower panel provides the image sensitivity relative to the natural array sensitivity for images with the most Gaussian possible dirty beam of the indicated FWHM for an 4h tracking observation. The central panel gives the dirty PSF RMS within the central 10x10 FWHM excluding the central positive lobe for an 8h track. The upper panel gives the dirty PSF RMS for a transit snap-shot.

8 Simulated Test Image Comparisons

While the plots shown in Figures 11 – 14 provide some indication for the anticipated imaging performance of the SKA1 configurations relative to other existing facilities, there is benefit in demonstrating the distinctions more graphically. To this end we have constructed several test images from high quality, wide area mosaics obtained with the Hubble Space Telescope. Images of bounded, astronomical objects and deep fields were sought that had the widest possible range of inherent spatial scales. Three images meeting these criteria were the 2224x2212 pixel Crab Nebula mosaic (Image Credit: NASA, ESA, J. Hester (Arizona State University)), the 2814x2844 pixel M83 mosaic (Image Credit: NASA, ESA, and the Hubble Heritage Team (STScI/AURA), W. Blair (STScI/Johns

Hopkins University) and R. O'Connell (University of Virginia)) and the 2300x2100 pixel Hubble Ultra Deep Field image (Image Credit: NASA, ESA, H. Teplitz and M. Rafelski (IPAC/Caltech), A. Koekemoer (STScI), R. Windhorst (Arizona State University), and Z. Levay (STScI)). These images, represented in a grayscale "png" format with integer brightness levels between $B = 0$ and 255, were given a nonlinear rescaling, $B' = 10^{[(B/255)]^n} - 1$, for several values of $n \geq 1$, to enhance the numerical dynamic range. The central object coordinates were arbitrarily modified and the pixel size was adjusted so that the Crab Nebula image spanned 4.1 degrees, the M83 image spanned 37 arcmin and the HUDF image 3.7 arcmin. This was done to match the object sizes to the approximate FWHM of the SKA1-Low station beam at 140 MHz in the first case, as well as the SKA1-Mid primary beam at 1.4 GHz for the second and 14 GHz for the third case. The three images were then interpolated via a cubic spline onto a three times more finely sampled grid and zero padded to a full image size of 16k by 16k pixels, thus ensuring that no more than the central quarter of the full image contains well-sampled emission features. Imaging simulations were then undertaken by multiplying the test images with a Gaussian approximation of the relevant primary beam and then forming the convolution of these large images with the identically sampled and equally large dirty PSFs of the telescope in question. It should be noted that these noiseless simulations only attempt to demonstrate the relative quality of dirty images. It should also be noted that no attempt was made to model calibration errors that would be present in any real observation, nor any time and bandwidth smearing effects that would be introduced by inadequate sampling of the visibilities relative to the field of view. In this sense, these are very much a "best case scenario".

The three test images are shown in Figures 15, 16 and 17 after rescaling, resampling and tapering with the relevant primary beam patterns. The Crab Nebula and M83 images were rescaled with $n=1$, which assigns significant power to the diffuse emission relative to more compact sources and has an intrinsic dynamic range of about 30dB. The HUDF field was rescaled with $n=3$, which assigns lower relative power to the diffuse emission and provides an intrinsic dynamic range of about 45dB.

While various simulations of both long track and snap-shot observations were undertaken, the most illuminating of some of the distinctions in image quality were provided by the case of continuum snap-shot observations.

The comparison of SKA1-Low and LOFAR continuum transit snap-shot dirty images is shown in Figures 18 and 19. For the purpose of the simulation, the LOFAR configuration has been located at a latitude of -54° , rather than its true latitude of $+54^\circ$. In both cases, a centre frequency of 140 MHz is assumed together with 30 spectral channels spaced by 1.4 MHz from one another. A target Gaussian dirty beam of 10 arcsec FWHM is specified during imaging for both arrays.

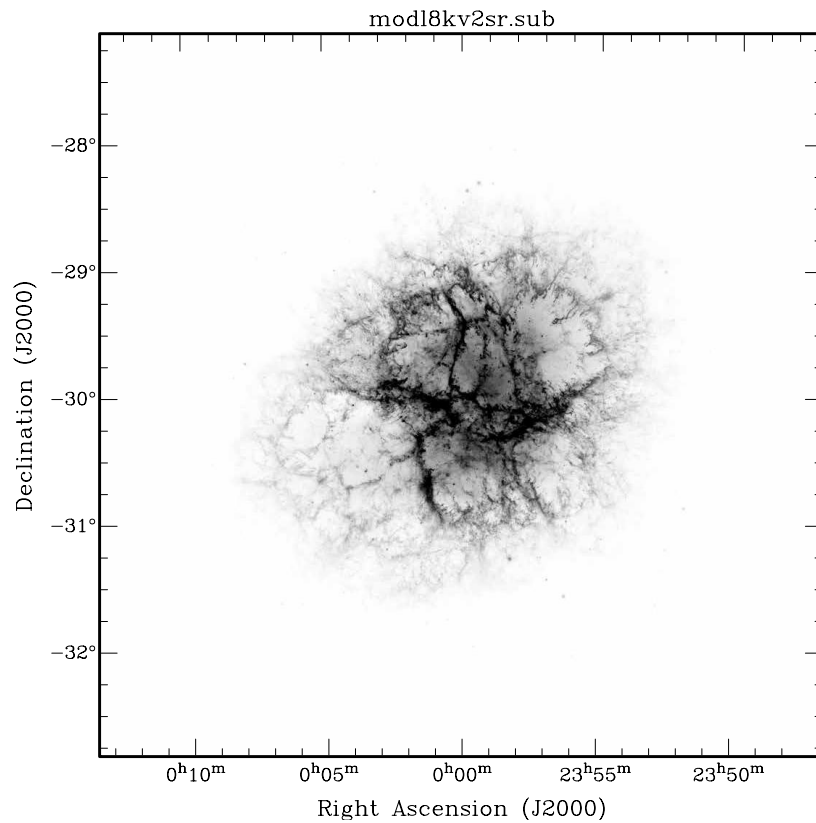


Figure 15. Test image, derived from the HST Crab Nebula image, for use with low frequency aperture array imaging simulations at 140 MHz.

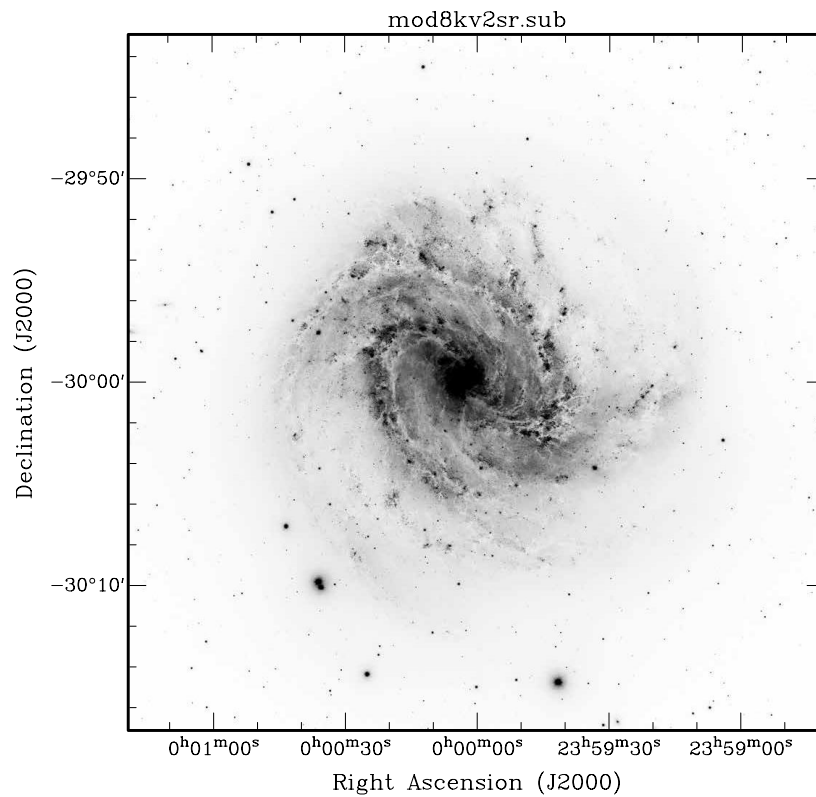


Figure 16. Test image, derived from the HST M83 image, for use with mid frequency dish array imaging simulations at 1.4 GHz.

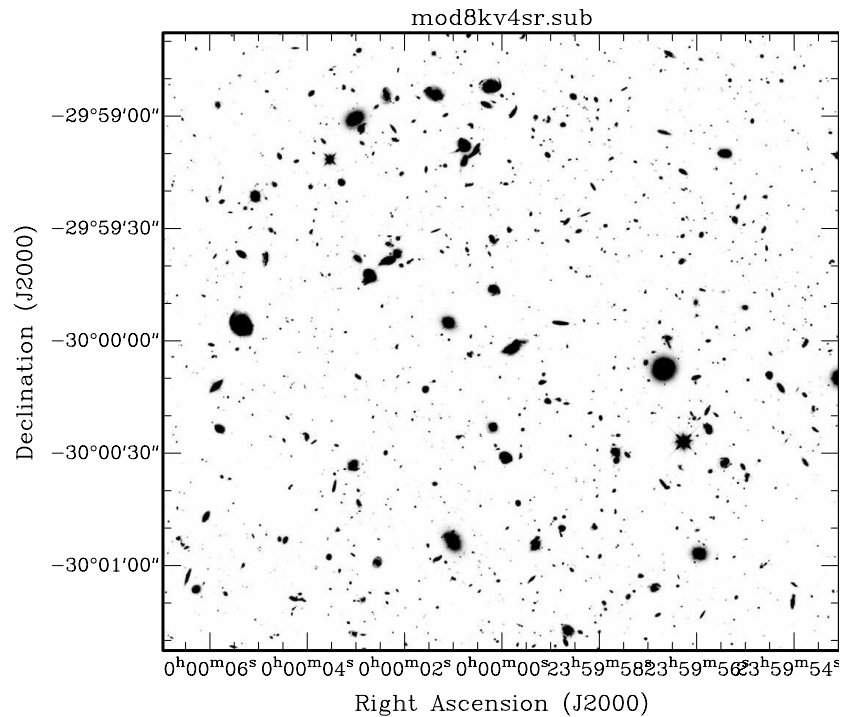


Figure 17. Test image, derived from the HST Ultra-Deep Field image, for use with mid frequency dish array imaging simulations at 14 GHz.

The first comparison of SKA1-Mid with VLA continuum transit snap-shot dirty images is shown in Figures 20 and 21. For the purpose of the simulation, the VLA configuration has been located at a latitude of -31° , rather than its true latitude of $+31^\circ$. In all cases, a centre frequency of 1.4 GHz is assumed together with 30 spectral channels spaced by 14 MHz from one another. A target Gaussian dirty beam of 1 arcsec FWHM is specified during imaging for all arrays. In the case of the VLA, the simulated observation includes four transit snap-shots; one in each of the A-, B-, C- and D-configurations.

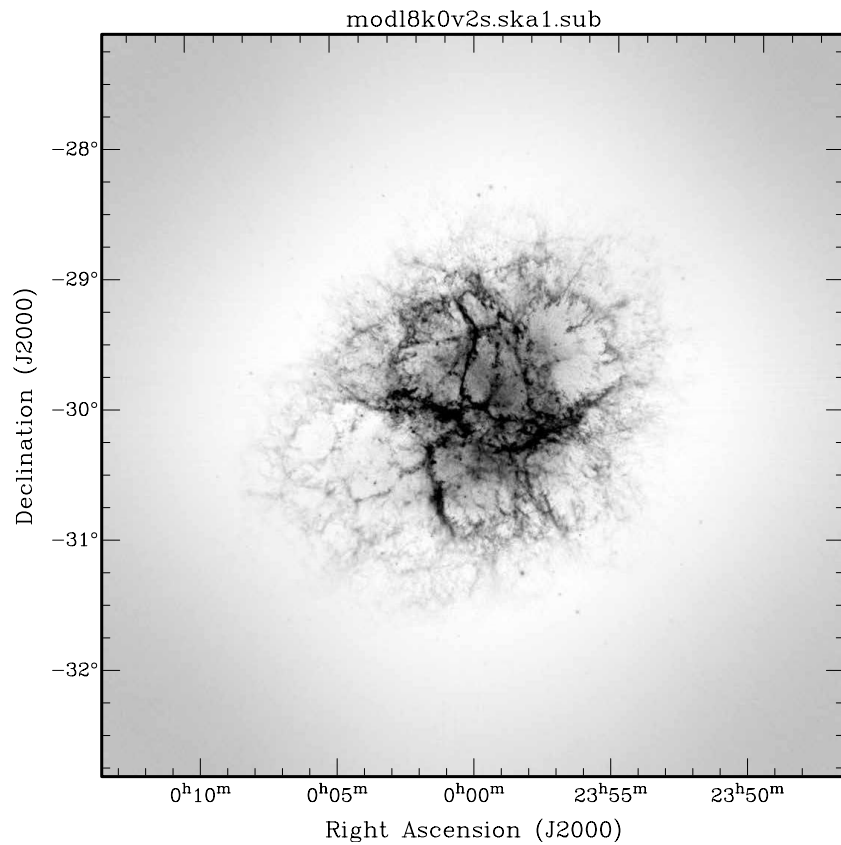


Figure 18. Simulated SKA1-Low continuum transit snapshot dirty image at 140 MHz.

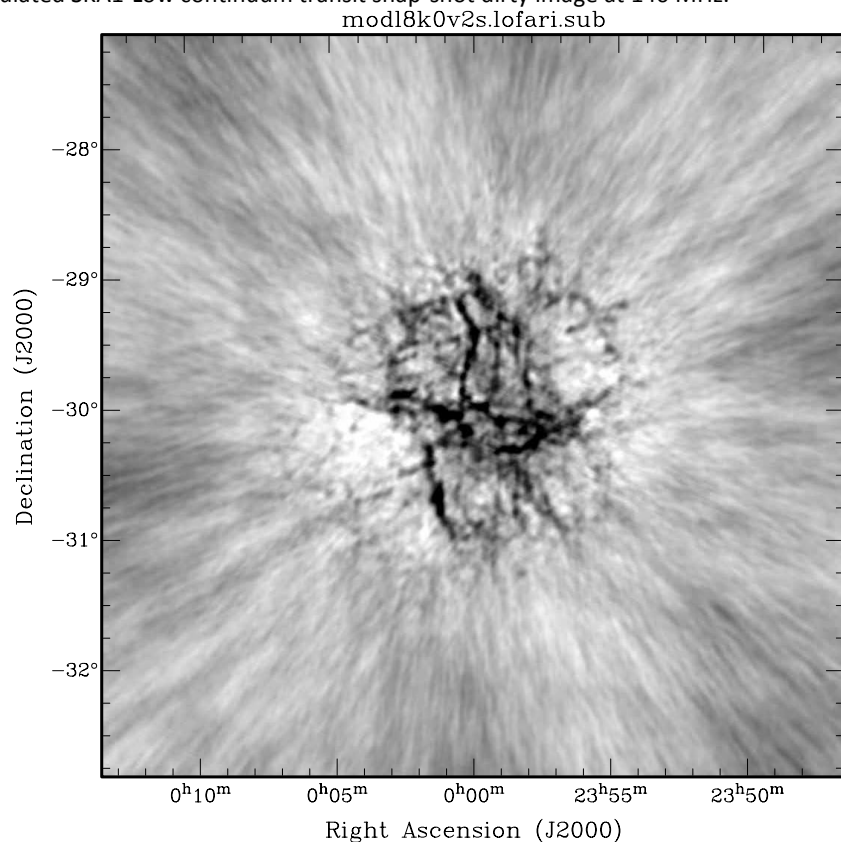


Figure 19. Simulated LOFAR continuum transit snapshot dirty image at 140 MHz.

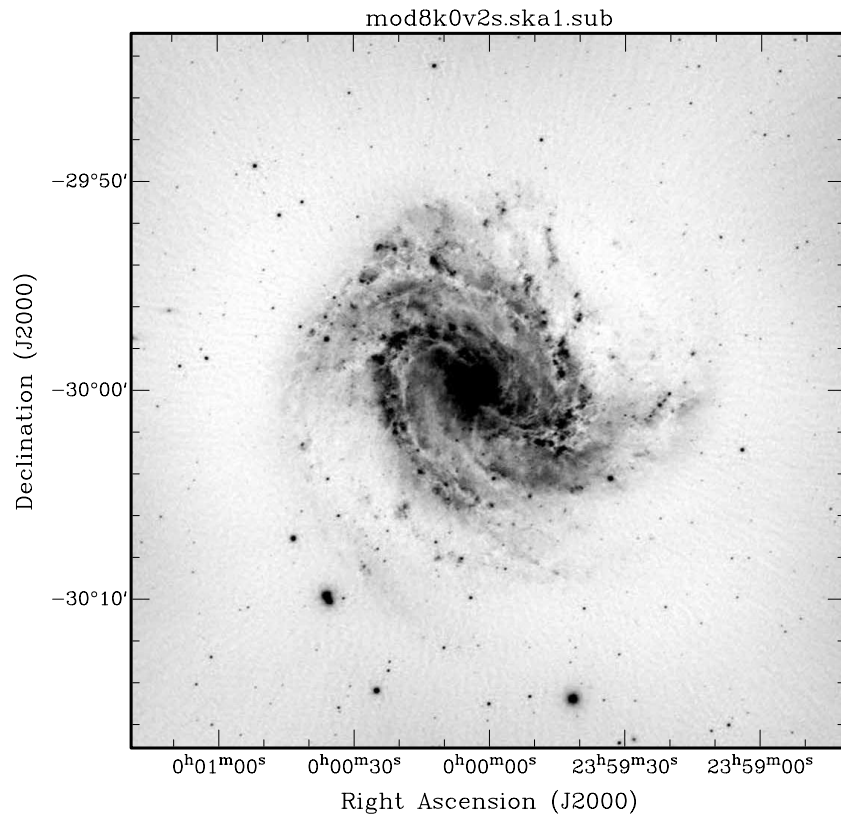


Figure 20. Simulated SKA1-Mid continuum transit snap-shot dirty image at 1.4 GHz.

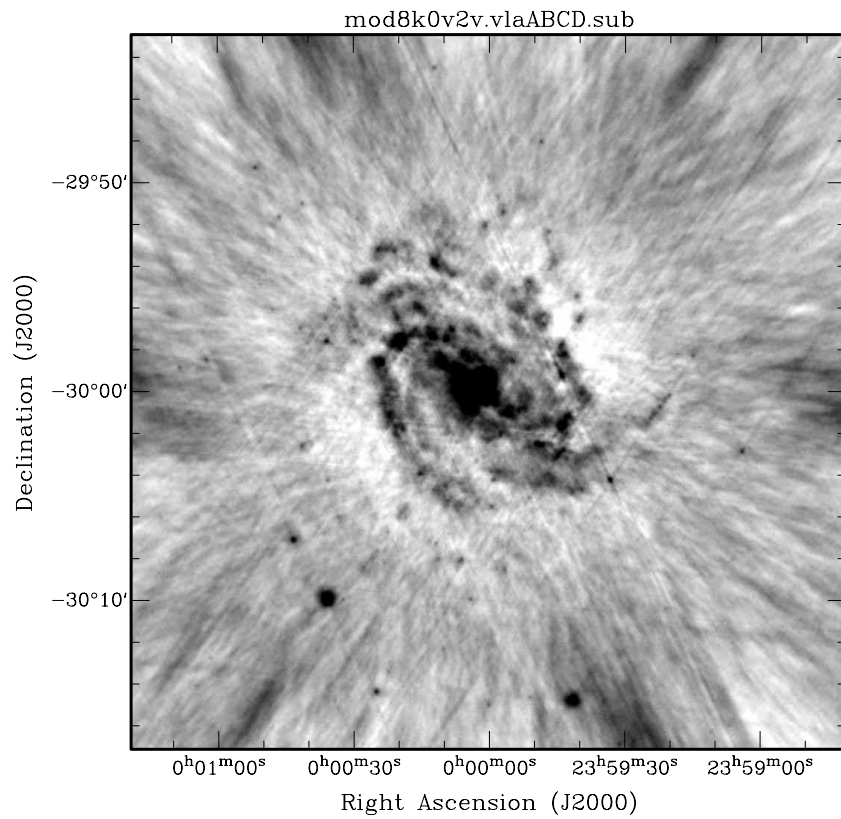


Figure 21. Simulated VLA continuum transit snap-shot A+B+C+D configuration dirty image at 1.4 GHz.

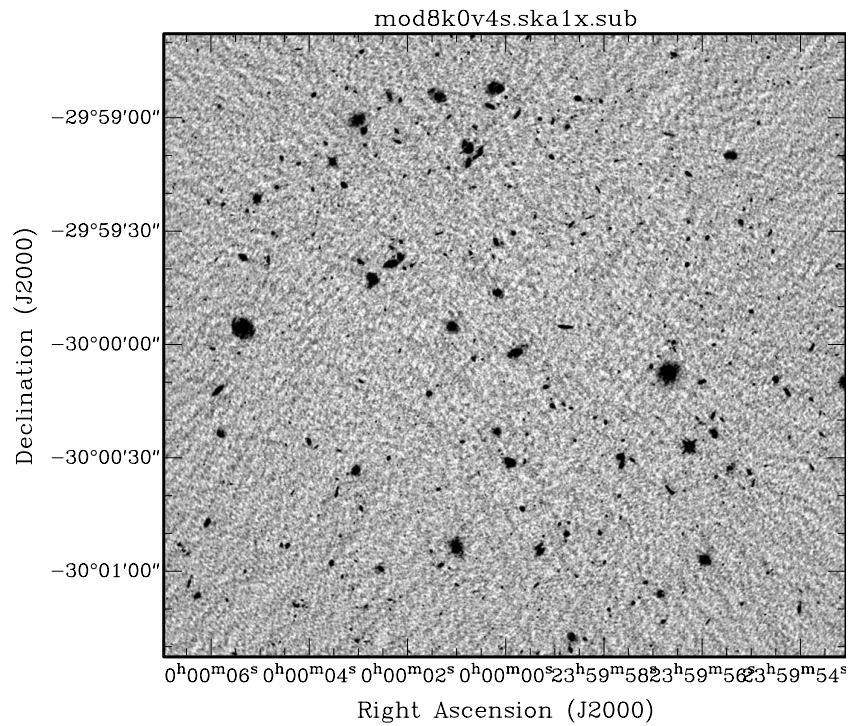


Figure 22. Simulated SKA1-Mid continuum transit snap-shot dirty image at 14 GHz.

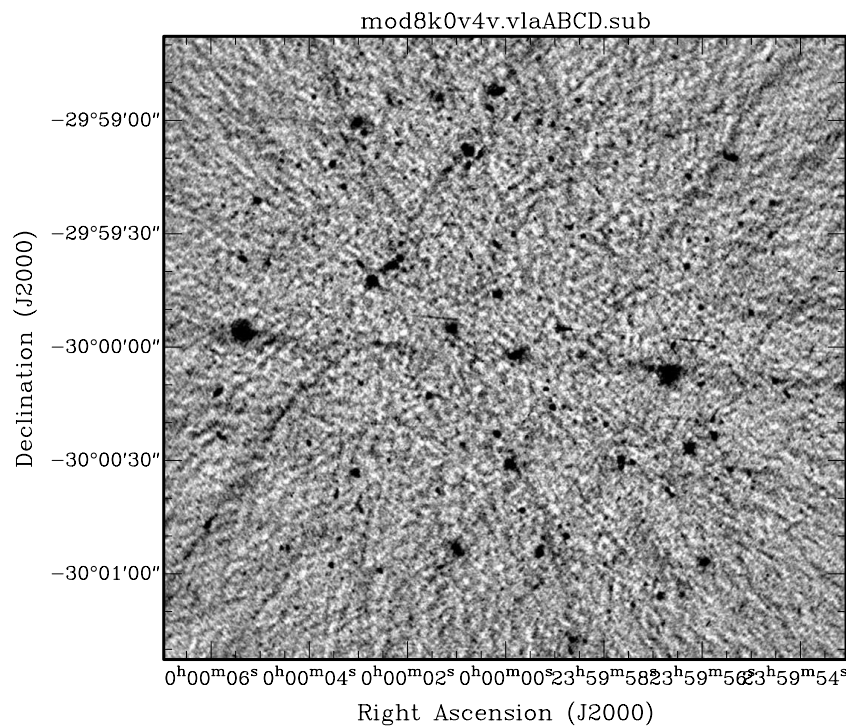


Figure 23. Simulated VLA continuum transit snap-shot A+B+C+D configuration dirty image at 14 GHz.

The second imaging comparison for SKA1-Mid is shown in Figures 22, 23 and 24. In this case, a centre frequency of 14 GHz is assumed together with 30 spectral channels spaced by 140 MHz from one another. A target Gaussian dirty beam of 0.1 arcsec FWHM is specified during imaging for all arrays. Unlike the previous case, where both the SKA and MeerKAT dishes were contributing to the visibility sampling, in this case only the 133 SKA1 dishes are assumed in the simulation. Since the intrinsic dynamic range of the test image was deliberately made rather high, the dirty snap-shot images (Figures 22 and 23) are quite limited in the depth that they reach. However, longer tracking observations, like the eight-hour track shown in Figure 24, can easily recover the full dynamic range of the model test image.

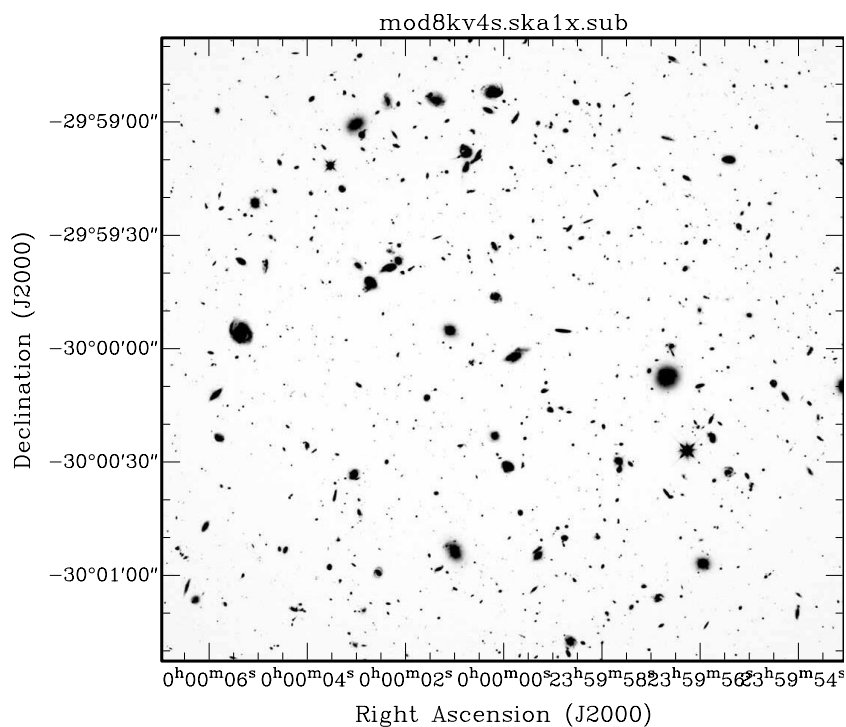


Figure 24. Simulated SKA1-Mid continuum eight-hour track dirty image at 14 GHz.

It is apparent from the sequence of imaging simulations that both SKA1-Low and SKA1-Mid will have an exceptional imaging capability relative to the interferometric arrays of today. Even short snapshot continuum observations will provide excellent fidelity for large and complex sources. When target fields have extremely high levels of intrinsic dynamic range, longer tracking observations will be needed for imaging. Given the excellent sampling of short baselines, only the very largest structures, relative to the primary beam size will require mosaic observations or total power measurements to supplement the visibilities obtained in a single pointing. Relative to LOFAR and even multi-configuration VLA imaging, one can anticipate between 10 and 100 times the image quality. In those cases where target sources are less than about half of the primary beam FWHM in extent and one is content with an angular resolution that does not require extrapolation beyond the measured visibility plane, it will typically not be necessary to rely on deconvolution to improve the image quality. Iterative modelling of the distribution of sources within the local sky model will of course still be necessary for the purposes of calibration and such modelling might well involve the use of deconvolution.

9 Wide-Band “Continuum” Observing

When quantifying the scientific performance of a facility for the study of broad-band continuum phenomena, there are a number of issues that need to be considered. First is the intrinsic SED (spectral energy distribution) of the target source population. Only a small fraction of the faint extragalactic source population can be described by a relatively flat spectral index, $\alpha \approx 0$, where $S_\nu = S_0 (\nu/\nu_0)^\alpha$ [cf. Figure 7 of RD14]. And even when this is the case, it is unlikely to be a good representation of the spectrum over a large fractional bandwidth. Other source populations vary between the ultra-steep negative spectra ($\alpha = -1 - -2$) of diffuse galaxy cluster sources as well as much of the pulsar population, to the ultra-steep positive spectra ($\alpha = +3 - +4$) for the modified black-body of dust emission sources. To document the scientific utility of broad-band observations we plot the signal-to-noise ratio for sources of varying spectral index as a function of the fractional bandwidth employed for the observation in Figure 22.

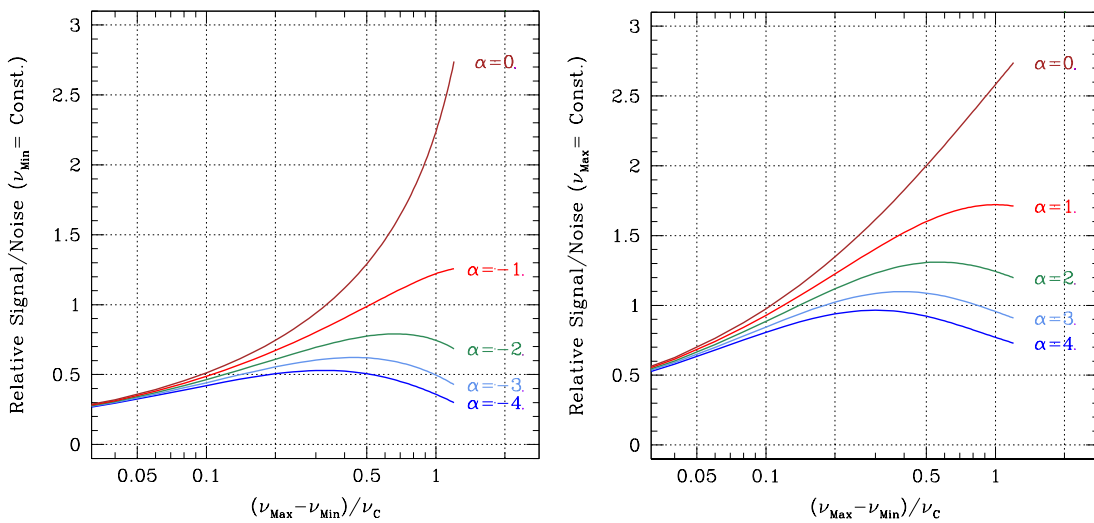


Figure 25. The relative signal-to-noise ratio as function of fractional bandwidth for varying spectral index of the source population. For negative spectral indices (left) the minimum observing frequency is kept fixed, while for positive spectral indices (right) the maximum observing frequency is kept fixed.

Since the largest signal contribution comes from the minimum observing frequency (for $\alpha < 0$) or the maximum observing frequency (for $\alpha > 0$) we keep this quantity fixed while varying the fractional bandwidth, $(\nu_{\text{Max}} - \nu_{\text{Min}}) / \nu_c$, in the plots. The curve for $\alpha = 0$ describes the typical assumption of an improvement in signal-to-noise that is proportional to the square root of bandwidth. As is apparent from the plots, there are significant departures from the square root bandwidth approximation for even modest values of the fractional bandwidth of 10 – 20%. For the more extreme spectral indices, the signal-to-noise ratio even declines for fractional bandwidths exceeding about 30%, since more noise than signal is then being averaged in the outcome. It is apparent from this demonstration that the practise of quoting continuum sensitivities based on a large fractional bandwidth is extremely misleading.

A second factor to consider when documenting the broad-band performance is the question of whether a single telescope pointing is being utilised for the observation of interest or whether a large area of the sky is being studied that requires multiple telescope pointings (as determined by the highest observing frequency under consideration). In the event that multiple telescope pointings are required, one must take account of the different noise effective field-of-view that is available as function of frequency. Since the FoV scales as ν^{-2} (as shown in Section 6), the density of pointings on the sky that is required to achieve a uniform net sensitivity on the sky is determined by the highest

observing frequency. Consequently, the degree of pointing over-sampling increases linearly in each direction toward lower frequencies, with the net effect that the survey sensitivity increases as ν^{-1} , for the case of an intrinsic sensitivity that is constant with frequency.

Finally, one must consider the intrinsic telescope variation of sensitivity with frequency itself, such as shown in Figure 7 and documented in Tables 3 and 4. For large fractional bandwidth, this variation can also become significant.

In view of all these considerations, we prefer to limit performance projections of broad-band continuum observations to no more than about 30% fractional bandwidth. However, as shown in Figure 21, even this limit will be overly optimistic in predicting the actual signal-to-noise by up to a factor of two for some plausible source populations.

10 Imaging Sensitivity

Given the array sensitivity documented in Section 5 together with the sensitivity as function of angular scale in Section 7 it is straightforward to provide estimates of the image sensitivity for specific observations. The SEFD (System Equivalent Flux Density) is given by, $SEFD = 2 k_B T_{sys}/A_{eff}$, where k_B is the Boltzmann constant. The image noise is given by,

$$\sigma = S_D SEFD / [\eta_s (n_{pol} \Delta\nu \Delta\tau)^{1/2}],$$

where S_D is a degradation factor relative to the natural array sensitivity for the specific target Gaussian FWHM resolution of the image. As discussed in Section 7, this degradation factor is approximately $S_D \approx 2$ for a wide range of intermediate angular scales and climbs to larger values for extreme angular scales. The factor η_s is a system efficiency that takes account of the finite correlator efficiency and other forms of incoherence and is assumed to be $\eta_s = 0.9$. The factor n_{pol} is the number of contributing polarisations and will be assumed to be $n_{pol} = 2$. The contributing bandwidth is $\Delta\nu$ and the integration time is $\Delta\tau$. For illustration, we will consider the cases of a spectral line observation with fractional bandwidth of $\Delta\nu/\nu_c = 10^{-4}$ and a continuum observation with fractional bandwidth of $\Delta\nu/\nu_c \approx 0.3$, together with an integration time $\Delta\tau = 1$ hour.

The image sensitivity for SKA1-Low and SKA1-Mid is listed in Tables 1 and 2, based on an assumed degradation factor (cf. Table 5) of $S_D = 2.5$ for σ_L and $S_D = 2$ for σ_C . The range of target Gaussian FWHM beam sizes over which this is assumed to apply is given by θ_{min} to θ_{max} . The beam sizes outside of this range which lead to a doubling of the RMS noise (to $S_D = 4$) are indicated by θ'_{min} and θ'_{max} . The spectral line sensitivity is the average over the frequency range indicated. The continuum sensitivity is estimated from the square root of the sum of the squared sensitivities over the indicated range. For SKA1-Low, we include an additional column labelled $\sigma_{conf}(\theta_{min})$, the confusion noise following RD17 that applies at the band centre frequency for the beam size, θ_{min} . As noted in §3.3, we assume that the MeerKAT dishes will only contribute to the image sensitivity of SKA1-Mid within the frequency ranges of the UHF, L and S bands. Outside of these ranges the array configuration is assumed to include only the SKA dishes.

Table 1. Image sensitivity of SKA1-Low within the indicated frequency bands for spectral line observations (σ_L for $\Delta\nu/\nu_c = 10^{-4}$) and continuum observations (σ_C for $\Delta\nu/\nu_c \approx 0.3$) for an observation of $\Delta\tau = 1$ hour. The range of Gaussian FWHM beam sizes for which the approximate sensitivity value applies is given by θ_{\min} to θ_{\max} . The Gaussian FWHM beam sizes at which a doubling of the image noise from this base level is realised are given by θ'_{\min} and θ'_{\max} . The anticipated confusion noise at a resolution θ_{\min} and ν_c is also listed (following RD17).

ν_{\min} (MHz)	ν_c (MHz)	ν_{\max} (MHz)	σ_L ($\mu\text{Jy/Bm}$)	σ_C ($\mu\text{Jy/Bm}$)	$\sigma_{\text{Conf}}(\theta_{\min})$ ($\mu\text{Jy/Bm}$)	θ'_{\min} (")	θ_{\min} (")	θ_{\max} (")	θ'_{\max} (")
50	60	69	11050	163	677	16.4	23.5	1175	3290
69	82	96	3261	47	183	11.9	17.0	850	2379
96	114	132	1841	26	50	8.6	12.3	614	1719
132	158	183	1258	18	13	6.2	8.9	444	1244
183	218	253	973	14	4	4.5	6.4	321	899
253	302	350	794	11	1	3.3	4.6	232	650

Table 2. Image sensitivity of SKA1-Mid within the indicated frequency bands for spectral line observations (σ_L for $\Delta\nu/\nu_c = 10^{-4}$) and continuum observations (σ_C for $\Delta\nu/\nu_c \approx 0.3$) for an observation of $\Delta\tau = 1$ hour. The range of Gaussian FWHM beam sizes for which the sensitivity values applies is given by θ_{\min} to θ_{\max} . The Gaussian FWHM beam sizes at which a doubling of the image noise from this base level is realised are given by θ'_{\min} and θ'_{\max} . The grey shading is used to approximately indicate those frequencies that are not yet part of the current deployment plan (ie. between 1.76 and 4.6 GHz as well as above 15.3 GHz).

ν_{\min} (GHz)	ν_c (GHz)	ν_{\max} (GHz)	σ_L ($\mu\text{Jy/Bm}$)	σ_C ($\mu\text{Jy/Bm}$)	θ'_{\min} (")	θ_{\min} (")	θ_{\max} (")	θ'_{\max} (")
0.35	0.41	0.48	1176	16.8	1.015	2.031	270.8	541.6
0.48	0.56	0.65	560	8.1	0.745	1.489	198.6	397.2
0.65	0.77	0.89	303	4.4	0.546	1.092	145.6	291.2
0.89	1.05	1.21	186	2.7	0.400	0.801	106.8	213.5
1.21	1.43	1.65	137	2.0	0.294	0.587	78.3	156.6
1.65	1.95	2.25	113	1.6	0.215	0.431	57.4	114.9
2.25	2.66	3.07	99	1.4	0.158	0.316	42.1	84.2
3.07	3.63	4.18	109	1.6	0.116	0.232	30.9	61.8
4.18	4.94	5.70	95	1.4	0.085	0.170	22.7	45.3
5.70	6.74	7.78	89	1.3	0.062	0.125	16.6	33.2
7.78	9.19	10.61	85	1.2	0.046	0.091	12.2	24.4
10.61	12.53	14.46	85	1.2	0.034	0.067	8.9	17.9
14.46	17.09	19.72	91	1.3	0.025	0.049	6.6	13.1
19.72	23.31	26.89	116	1.7	0.018	0.036	4.8	9.6
26.89	31.78	36.67	121	1.8	0.013	0.026	3.5	7.0
36.67	43.33	50.00	209	3.2	0.010	0.019	2.6	5.2

11 Non-Imaging Sensitivity

Many applications do not make use of the correlated visibilities, but instead rely on a tied array beam. A variable number of dishes or stations can contribute to the tied array beam sensitivity, ultimately constrained by the beam former design to lie within a region of 20km in diameter in the case of SKA1-Low and, for some applications, the entire array for SKA1-Mid. The specific choice will depend on various factors, including the observing frequency, which will influence the anticipated residual phase errors of the real-time calibration, as well as whether the observation is part of a search or directed at a target of known position and extent. Two illustrative examples are given by the radius within which approximately half of the total collecting area is concentrated, of about 1 km, and the maximum radius that is supported by the SKA1-Low beam former, of 10 km. The smaller radius should be compatible with minimal coherence loss due to uncalibrated ionospheric or atmospheric phase fluctuations under all but the most extreme of circumstances.

11.1 Non-Imaging Sensitivity for SKA1-Low

The tied array beam sensitivity as function of the maximum radius from the centre of the array configuration and observing frequency for SKA1-Low is shown in the left-hand panel of Figure 22. The SEFD as function of frequency for two reference radii, of one and ten km, is also shown in the right-hand panel of the figure.

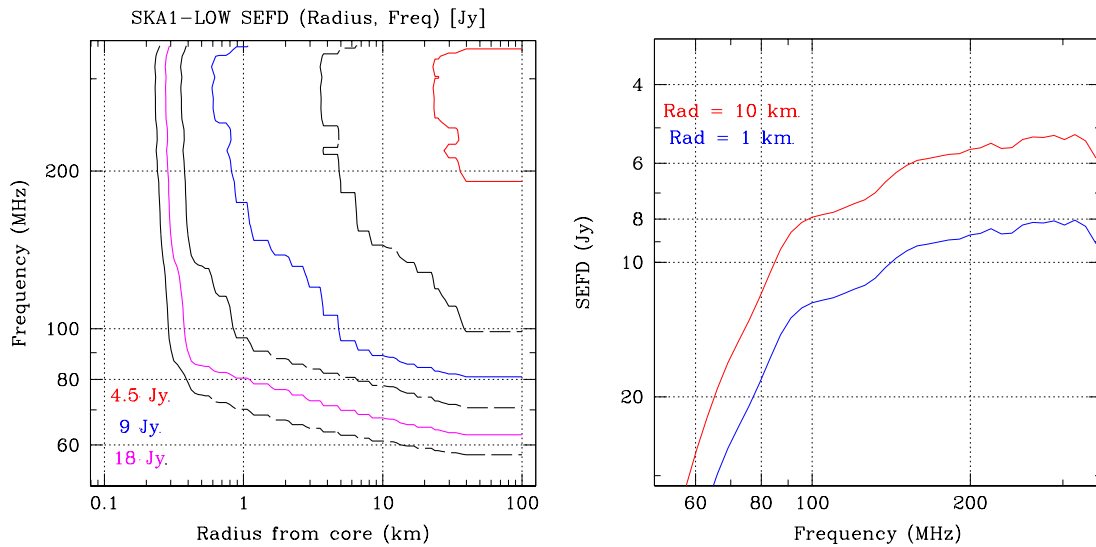


Figure 26. The tied array sensitivity of SKA1-Low as function of the maximum radius of included stations (left) as well as the sensitivity as function of frequency for two reference radii (right). The model is appropriate for an average elevation within 45 degrees of zenith in a direction well away from the Galactic plane.

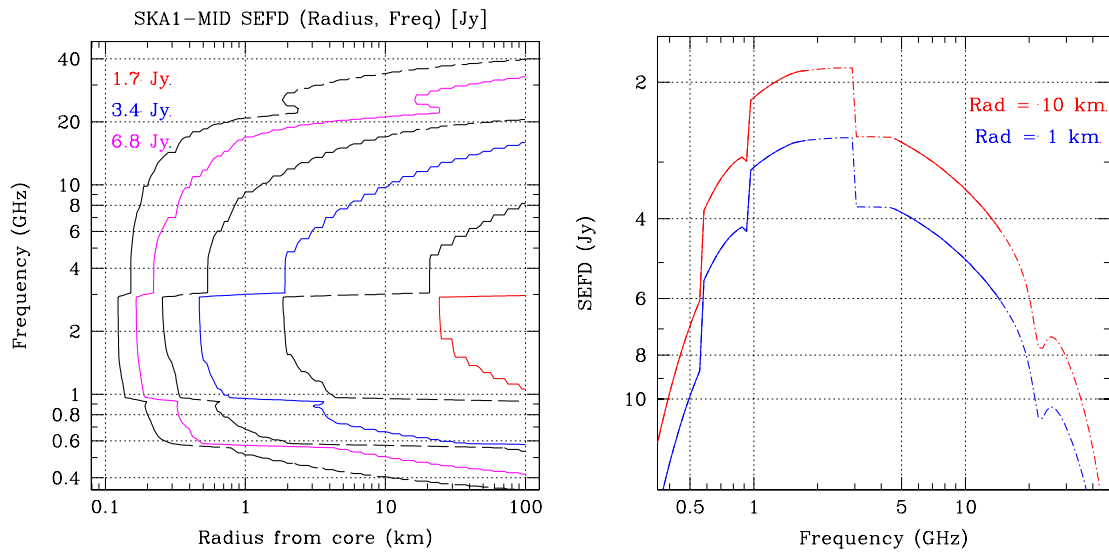


Figure 27. The tied array sensitivity of SKA1-Mid as function of the maximum radius of included dishes (left) as well as the sensitivity as function of frequency for two reference radii (right). The model is appropriate for elevations near zenith in a direction well away from the Galactic plane (the 10th percentile) and under dry conditions (PWV = 5mm). Solid lines (right) are used to indicate the bands that are part of the currently planned deployment.

11.2 Non-Imaging Sensitivity for SKA1-Mid

The tied array beam sensitivity as function of the maximum radius from the centre of the array configuration and observing frequency for SKA1-Mid is shown in the left-hand panel of Figure 23. The SEFD as function of frequency for two reference radii, of one and ten km, is also shown in the right-hand panel of the figure.

12 Additional SKA1-Mid Feed Systems

As noted in Section 3, although the sensitivity model developed for SKA1-Mid extends continuously from 350 MHz to 50 GHz, only a subset of the feed systems that would provide this coverage have advanced designs that are planned for deployment at this time. The three frequency bands currently planned for deployment are Bands 2, 5 and 1. Together, these provide coverage from 350 MHz to 1.76 GHz and from 4.6 to 15.3 GHz. As discussed in RD3, the cryostat designed for the high frequency bands will in the first instance be outfitted only with the Band 5a and 5b systems. However, it is being designed with additional cooling capacity and mounting locations such that at least three additional feed systems, notionally the Bands 3, 4 and 5c, could be retro-fitted to fill in the coverage between 1.76 and 4.6 GHz as well as extend it above 15.3 GHz. Deployment of such additional feed systems would provide an extremely cost effective means of extending the SKA1-Mid performance, should additional funding become available. The choice of which frequency bands to add would be determined by community interest. As discussed in Section 3, both the dish structure and the site are anticipated to enable good performance up to about 50 GHz. The relative dish pointing, under precision conditions, is anticipated to be 1.3 arcsec RMS (from RD4) which would also support good performance up to high frequencies.

13 Appendix A

The numerical values shown in several key plots are listed here in Table form for convenience. The individual SKA1-Low station and the combined SKA1-Low array natural sensitivities from Figure 7 are shown in Table 3. Recall, that these are averaged over all solid angles within 45 degrees of zenith. The individual SKA1-Mid dish and the combined SKA1-Mid array natural sensitivities from Figures 4 and 7 are shown in Table 4. The imaging sensitivity provided by the SKA1-Low and SKA1-Mid array configurations as function of scale, as plotted in Figures 11, 12, 13 and 14, is listed in Table 5.

Table 3. The individual SKA1-Low station and the combined SKA1-Low array natural sensitivities from Figure 7 are listed here as function of frequency. The sensitivity is averaged over solid angles within 45 degrees of zenith.

Frequency (MHz)	SKA1-Low Station Aeff/Tsys (m ² /K)	SKA1-Low Array Aeff/Tsys (m ² /K)
50	0.102	52.2
60	0.255	130.3
70	0.420	214.8
80	0.580	296.9
90	0.781	399.7
100	0.862	441.3
110	0.885	453.1
120	0.924	472.9
130	0.965	493.9
140	1.052	538.4
150	1.119	572.8
160	1.159	593.3
170	1.171	599.7
180	1.190	609.1
190	1.195	612.0
200	1.223	626.4
210	1.235	632.4
220	1.263	646.5
230	1.226	627.5
240	1.234	631.7
250	1.282	656.4
260	1.304	667.9
270	1.297	664.2
280	1.306	668.8
290	1.314	672.5
300	1.289	660.0
310	1.294	662.4
320	1.327	679.4
330	1.286	658.6
340	1.204	616.7
350	1.156	591.8

Table 4. The individual SKA1-Mid dish and the combined SKA1-Mid array natural sensitivities from Figures 4 and 7 are listed here as function of frequency. The grey shading is used to indicate frequencies that are not yet part of the current deployment plan. Note that the MeerKAT dishes are only assumed to contribute to the array sensitivity within the UHF, L and S Bands as described in Section 3.

Frequency (GHz)	SKA1-Mid Dish Aeff/Tsys (m2/K)	SKA1-Mid Array Aeff/Tsys (m2/K)
0.3508	2.208	293.7
0.3673	2.424	322.3
0.3846	2.648	352.2
0.4027	2.879	382.9
0.4217	3.114	414.2
0.4416	3.353	445.9
0.4624	3.594	478.1
0.4842	3.837	510.4
0.507	4.078	542.4
0.5309	4.316	574
0.5559	4.55	605.1
0.5821	4.779	677.1
0.6095	5	918.2
0.6383	5.209	957.4
0.6683	5.404	994.4
0.6998	5.581	1029
0.7328	5.737	1060
0.7674	5.869	1088
0.8035	5.971	1112
0.8414	6.037	1130
0.881	6.072	1144
0.9226	6.071	1124
0.9661	9.324	1567
1.012	9.47	1597
1.059	9.59	1623
1.109	9.698	1647
1.161	9.796	1671
1.216	9.883	1693
1.274	9.961	1713
1.334	10.03	1733
1.396	10.09	1751
1.462	10.15	1767
1.531	10.2	1781
1.603	10.24	1792
1.679	10.28	1799
1.758	10.31	1804
1.841	10.34	1810
1.928	10.37	1814
2.018	10.39	1818
2.113	10.41	1821
2.213	10.42	1824
2.317	10.44	1826
2.427	10.45	1828

2.541	10.46	1829
2.661	10.46	1830
2.786	10.47	1831
2.917	10.46	1830
3.055	10.46	1392
3.199	10.46	1392
3.35	10.46	1392
3.508	10.46	1391
3.673	10.46	1391
3.846	10.45	1390
4.027	10.45	1390
4.217	10.44	1389
4.416	10.43	1388
4.624	10.36	1378
4.842	10.25	1363
5.07	10.13	1348
5.309	10.01	1332
5.559	9.891	1315
5.821	9.764	1299
6.095	9.633	1281
6.383	9.5	1263
6.683	9.362	1245
6.998	9.222	1226
7.328	9.078	1207
7.674	8.931	1188
8.035	8.78	1168
8.414	8.617	1146
8.81	8.461	1125
9.226	8.299	1104
9.661	8.138	1082
10.12	7.97	1060
10.59	7.801	1038
11.09	7.617	1013
11.61	7.446	990.3
12.16	7.267	966.5
12.74	7.084	942.2
13.34	6.89	916.4
13.96	6.7	891.1
14.62	6.497	864.1
15.31	6.295	837.3
16.03	6.078	808.4
16.79	5.85	778
17.58	5.597	744.4
18.41	5.317	707.2
19.28	4.985	663
20.18	4.564	607
21.13	4.043	537.7
22.13	3.587	477.1
23.17	3.574	475.3

24.27	3.726	495.6
25.41	3.791	504.3
26.61	3.751	498.9
27.86	3.648	485.2
29.17	3.507	466.4
30.55	3.337	443.9
31.99	3.163	420.6
33.5	2.971	395.1
35.08	2.77	368.4
36.73	2.562	340.8
38.46	2.348	312.2
40.27	2.122	282.2
42.17	1.883	250.4
44.16	1.626	216.2
46.24	1.345	178.9
48.42	1.027	136.6

Table 5. The imaging sensitivity degradation relative to the natural array sensitivity provided by the SKA1-Low and SKA1-Mid array configurations as plotted in Figures 11, 12, 13 and 14 is listed as a function of the FWHM of the most Gaussian possible dirty beam provided by a (4h for Low and 8h for Mid) tracking observation at a reference frequency (140 MHz for Low and 1.4 GHz for Mid). Image attributes at any other frequency can be inferred by a linear scaling to higher or lower angular scales for higher or lower frequencies. The Sens*/Nat columns for SKA1-Mid are relevant for frequencies at which the MeerKAT dishes do not contribute to the array

Low Line		Low Cont		Mid Line			Mid Cont		
FWHM (arcsec)	Sens /Nat	FWHM (arcsec)	Sens /Nat	FWHM (arcsec)	Sens /Nat	Sens* /Nat	FWHM (arcsec)	Sens /Nat	Sens* /Nat
6.6	5.0	4.7	11.0	0.3	5.0	3.7	0.2	10.3	9.2
7	4.7	4.8	8.6	0.4	4.1	3.1	0.3	3.4	3.1
9.4	3.2	6.7	4.2	0.7	3.2	2.5	0.6	2.0	1.9
12	3.0	10	2.3	1	3.2	2.6	1	1.9	1.9
21	2.7	20	2.0	2	2.9	2.6	2	1.9	1.9
32	2.7	30	2.0	3	2.7	2.5	3	1.8	2.0
53	2.7	49	1.9	5	2.3	2.5	5	1.6	2.0
105	2.5	98	2.0	10	2.1	2.5	10	1.5	2.1
197	2.2	196	2.1	20	2.1	2.6	20	1.5	2.1
295	2.0	295	2.0	30	1.9	2.5	30	1.5	2.0
491	2.0	491	2.0	49	1.9	2.4	49	1.6	2.1
983	3.1	983	3.0	98	2.8	2.9	98	2.3	2.6
1980	5.5	2020	5.4	196	6.3	5.4	196	5.2	5.3
2875	8.0	2874	7.7	293	11.9	9.7	284	10.7	10.0
4720	13.4	4750	12.8	465	27.1	21.5	468	26.0	23.6
6260	23.4	6550	23.8	720	80.8	66.0	768	97.2	78.6

14 Appendix B

Key performance data from the reference documents is gathered here for convenience. The anticipated performance of an SKA1 dish equipped with the Band 1 feed system is shown in Figure 24, reproduced from Figure 8 of RD1.

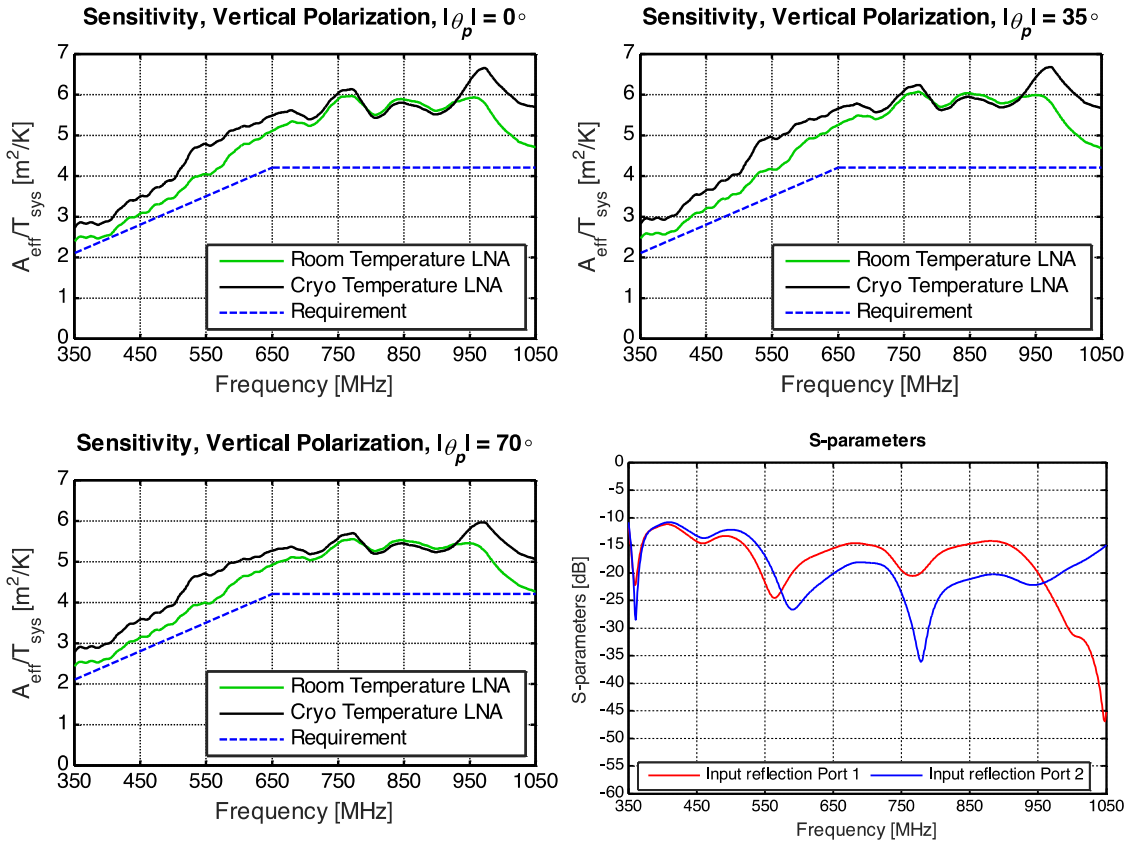


Figure 28. Sensitivity of an SKA1 dish equipped with SPF Band 1, reproduced from Figure 8 of RD1.

Similarly, the anticipated performance of the Band 2 feed system is shown in Figure 25, reproduced from Figure 21 of RD16. Finally, the anticipated performance of the Band 5a and Band 5b feed systems is shown in Figure 26, reproduced from Figures 78 and 79 of RD3. The figure shown here for the Band 5a feed system has been updated by the authors of RD3.

The composite sensitivity model for both the SKA1 dish and the MeerKAT dish is shown overlaid on the referenced data (RD1, RD3 and RD16 for the SKA and RD7 for MeerKAT) in Figure 27.

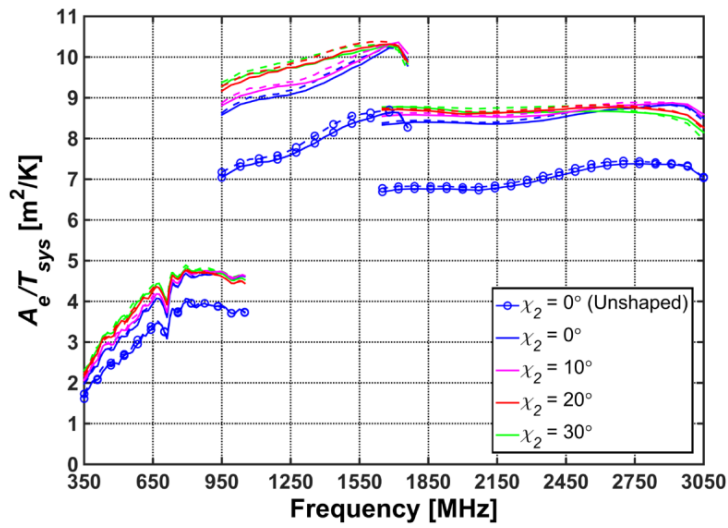


Figure 29. Sensitivity of an SKA1 dish equipped with SPF Band 2, reproduced from Figure 21 of RD16.

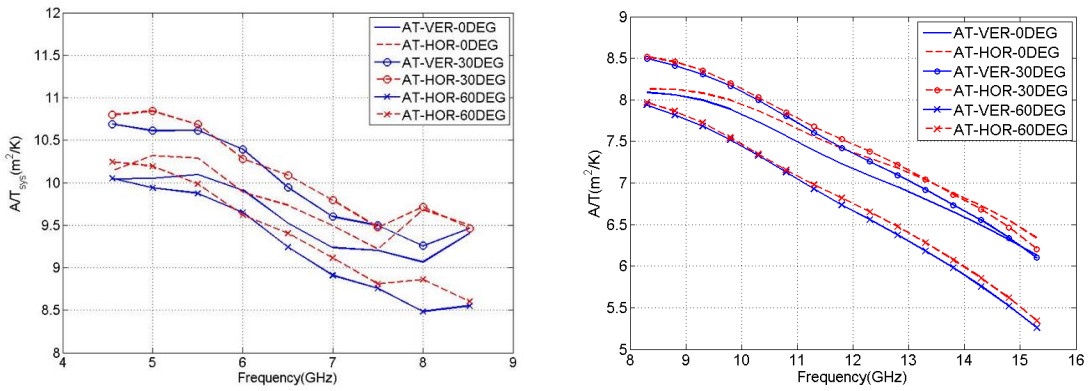


Figure 30. Sensitivity of an SKA1 dish equipped with SPF Band 5a (left) and 5b (right), reproduced from Figures 78 and 79 of RD3 and in the case of the Band 5a feed has been updated by the authors.

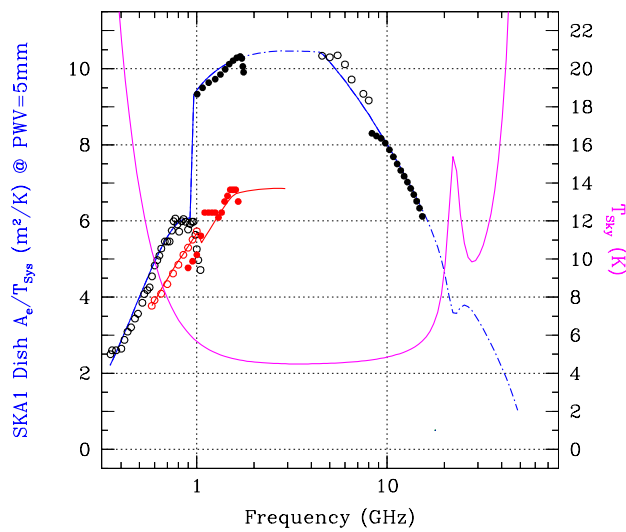


Figure 31. Overlay of the SKA1 dish (in blue) and MeerKAT dish (in red) sensitivity models with the referenced data.